December 2020

Dislocation Slip and Deformation Twinning in Face Centered Cubic Low Stacking Fault Energy High Entropy Alloys

Mitra Shabanisamghabady
Clemson University, mitra.shabani1991@gmail.com

DISLOCATION SLIP AND DEFORMATION TWINNING IN FACE CENTERED CUBIC LOW STACKING FAULT ENERGY HIGH ENTROPY ALLOYS

A Dissertation
Presented to
the Graduate School of
Clemson University

In Partial Fulfillment
of the Requirements for the Degree
Doctor of Philosophy
Mechanical Engineering

---

by
Mitra Shabani
December 2020

Accepted by:
Dr. Garrett Pataky, Committee Chair
Dr. Huijuan Zhao, Committee Co-chair
Dr. Gang Li, Committee member
Dr. Qiushi Chen, Committee member

ABSTRACT

There is an ongoing need for the design and development of metal alloys with improved properties for extreme environment applications. High entropy alloys (HEAs) are a group of metal alloys that in contrary to conventional metal alloys can have multiple principal elements in high concentrations. HEAs show promising properties better than or comparable to conventional metal alloys for a range of temperature down to cryogenic temperature. HEAs are good candidates to be used as structural materials for extreme environments applications such as in aerospace, automotive, transportation, and energy industries, among others. Mechanical behavior and the underlying plastic deformation mechanisms and the factors affecting HEAs need to be fully understood to be able to use these alloys for the mentioned applications and to design and develop further improved metal alloys.

Low stacking fault energy face centered cubic (fcc) HEAs show simultaneous high strength and ductility and specially by the decrease in temperature down to cryogenic temperatures, whereas there is usually a tradeoff between strength and ductility in conventional metal alloys. Plastic deformation in low stacking fault energy fcc HEAs starts with dislocation slip and with the increase in stress, deformation twins nucleate and grow as an additional mode of deformation. There have been studies that experimentally and computationally looked at slip and deformation twins and the effect of different parameters on their nucleation and growth in HEAs. However, the critical resolved shear stress for slip which indicates the beginning of the plastic deformation region in some of these HEAs has not been found. Also, different factors in deformation twin nucleation and growth have

been studied but the effect of grain boundary (GB) types and elemental segregation at GBs have not been fully investigated.

In this research experimental and computational approaches are used to further identify the underlying plastic deformation mechanisms in HEAs giving rise to their improved properties. High resolution digital image correlation and electron backscatter diffraction have been used to find the dislocation slip critical resolved shear stress (CRSS) in $Al_{0.3}$CoCrFeNi polycrystalline under tension. Molecular dynamics (MD) simulations and Monte Carlo molecular dynamics (MCMD) simulations have been used to identify the effect of different symmetric twist GB types and elemental segregation on deformation twins in CoCrFeNi bicrystals at three different temperatures 77 K, 100 K, and 300 K.

Experimentally $Al_{0.3}$CoCrFeNi polycrystalline was tested under tension at room temperature slip CRSS was found to be 63±2 MPa based on the activated slip system of (-1 1 1)[-1 -1 0] which also had the highest Schmid factor of 0.42. The MD simulations and the MCMD simulations studies on the CoCrFeNi HEA bicrystals confirmed GBs as deformation twin nucleation sites. The mechanical properties and deformation twin nucleation changed with different symmetric twist GBs having different sigma values and misorientation angles. MCMD simulations revealed GBs becoming Cr-rich and Ni-deficient which matches the results from experimental observations and MCMD simulations of HEAs of similar compositions. Temperature also was shown to influence the material properties in this alloy. With the decrease in temperature from 600 K, to 300 K, to 77 K, the yield strength and stress, and the overall plastic flow stress increased, and the modulus of elasticity decreased. The mentioned scientific contributions guide HEA

design and development with improved properties through GB engineering by populating the polycrystals with symmetric twist grain boundaries of high angle misorientation angles and segregation engineering and designing chromium-rich GBs. As a next step to this research, experimentally, tensile tests at cryogenic temperatures with further post-mortem microscopy can be performed to find the CRSS at cryogenic temperatures and characterize the slip and deformation twins. Computationally, MCMD chemical equilibrium can be continued and reinforcement learning algorithms can be implemented to optimize the process. Furthermore, other types of GBs can be considered and the effect of GB geometry on the elemental segregation itself can be another route branching from this research.

DEDICATION

I dedicate this dissertation to my parents Dr. Mohammadali Shabani and Dr. Soudabeh Bahri Yekta, to my sister Mahsa Shabani and to Shahab Karimi for being there for me throughout my PhD journey.

Specially I want to dedicate this dissertation to my late grandmother, Marzieh Askarieh (Oma) who has always supported me and encouraged me to do the best I can in life.

ACKNOWLEDGMENTS

I would like to thank my advisor Dr. Garrett Pataky for his endless support throughout my experience at Clemson University. Dr. Pataky has always been supportive, and I admire his leadership and mentorship methods. I would like to thank my co-advisor Dr. Huijuan Zhao for her support and mentorship. I learned a lot from Dr. Zhao in the classroom and in the advising meetings. I would like to thank my committee members Dr. Gang Li and Dr. Qiushi Chen for their support.

I would like to thank my parents and my sister for their support and guidance and for being understanding. I would like to thank my relatives, and my friends for being supportive, and encouraging, among them, Moloud Nasiri, Mastooreh Seyyedi, Maryam Abdi, Haleh Barmaki, Nafise Masoudi, and Mahsa Kiani. I would like to thank Shahab Karimi for always supporting me and being there for me.

I would like to thank Dr. Summers for helping me find my way to continue my PhD studies, for his mentorship, and for providing opportunities for students like me with an interest in joining academia. I would like to thank Dr. Abdeljawad for his mentorship in research and in teaching techniques.

I would like to acknowledge my lab mates in the FRAME lab who have become my friends since joining the lab in August 2017, Kaitlynn Conway, Matt Williams, Jacob Biddlecom, Jody Bartanus, Cameron Abarotin, Benjamin Smith, Fredrick Monroe, and Muhammed Kose.

I would like to thank my fellow TAs and my students. I learned a lot from my fellow TAs and from my students throughout my experience as the graduate laboratory assistant and instructor of record.

I would like to acknowledge Clemson University mechanical engineering department faculty and staff for all the help and support. I would like to acknowledge Clemson University Electron Microscopy Facility personnel. Clemson University is acknowledged for generous allotment of compute time on Palmetto cluster.

I would like to acknowledge Dr. Jablonski and Dr. Liaw for providing the materials used in the experimental portion of this research.

TABLE OF CONTENTS

LIST OF TABLES

LIST OF FIGURES

CHAPTER ONE: INTRODUCTION

Parts of this section has been used as part of a journal paper.

1.1 Background and Motivation

There is an ongoing and increasing need of materials for extreme environment applications to assist with the advancement in technology. Therefore, development of materials with a combination of ideal properties for a wide range of external conditions is desirable. High entropy alloys (HEAs) are a group of metal alloys with properties better than or comparable to conventional metal alloys, making them good candidates as structural materials under extreme conditions [1–5]. HEAs consist of multiple principal elements in high concentrations whereas conventional techniques of alloying use one or two main elements with small amount of secondary elements to tailor the alloy to have desirable material properties [6–10].

In conventional metal alloys there is a tradeoff between the strength and ductility which are both desirable properties for structural material. In a group of HEAs called the 3d transition metal HEAs, both high strength and high ductility can be achieved with simultaneous improvement as the temperature decreases [1,2,11–14]. Also, alloying these HEAs with aluminum results in high yield strength among other desirable properties [15–18]. The main plastic deformation mode in these HEAs is dislocation slip, and the simultaneous improvement has been attributed to the activation of deformation nanotwins as an additional mode of plastic deformation mode [2,4,19,20]. In order to use HEAs in different applications, such as aerospace, automotive, and thin film, it is important to fully characterize and understand the plastic behavior and its underlying phenomena for these HEAs. Also, this knowledge can further help with designing and developing materials needed for next generation engineering applications in automotive and aerospace

industries and as structural materials in aggressive environments through populating the microstructure with preferential grain boundaries for deformation twin nucleation.

1.2 High entropy alloys

Conventional alloying specifically to achieve single-phase materials, starts from one or two main elements and secondary elements are added in small quantities to modify and improve the properties [21]. Using this approach, the alloys designed and developed are restricted and limited to the possible number of combinations [21]. With an ongoing need for materials with novel properties to meet technological challenges, unconventional alloying methods have been gaining interest in the recent decades.

With the idea of mixing multiple principal elements in high concentrations, Cantor et al. and Yeh et al. introduced HEAs in 2004 [6,22]. Cantor *et al.* focused on exploring the possibility of multicomponent materials and alloys with many different components at equiatomic percentages and discovered the single-phase face centered cubic (fcc) HEA CoCrFeMnNi, now commonly known as the Cantor alloy [6]. Yeh et al. on the other hand focused on the idea of developing simple solid solution alloys containing at least 5 elements with concentrations varying from 5 to 35 atom% in order to achieve alloys with high configurational entropy [22]. Configurational entropy increases with having large number of elements in high concentrations which decreases the Gibbs free energy [21]. The equations of the configurational entropy [10] and the Gibbs free energy [23] are as follows:

$$\Delta S_{mix} = -R \sum_{i=1}^{n} X_i ln X_i \qquad (1)$$

where ΔS_{mix} is the configurational entropy of mixing for the alloy, X_i is the more fraction for each of the elements, n in the number of elements, and R is the Boltzmann constant.

$$\Delta G_{mix} = \Delta H_{mix} - T\Delta S_{mix} \qquad (2)$$

where ΔG_{mix} is the change in the Gibbs free energy, ΔH_{mix} is the change in the system enthalpy, T is the temperature in Kelvin and ΔS_{mix} is the configurational entropy of mixing of the system.

In developing HEAs, in order to achieve crystalline solid solutions contributing to the ductility and toughness of the alloy, elements with small differences in the atomic size and enthalpies of mixing have been considered. A parameter has been proposed by Zhang et al. [24] as a design consideration in the development of HEAs besides the entropy of configuration and enthalpy of mixing which is based on the atomic size of each element. This parameter is called the atomic size difference δ and is found using the following equation:

$$\delta\% = 100\% \sqrt{\sum_{i=1}^{n} c_i \left(1 - \frac{r_i}{\sum_{j=1}^{n} c_j r_j}\right)^2} \qquad (3)$$

where *n* is the number of elements, c_i and c_j are the compositions of the *i*th and *j*th elements, and r_i and r_j are the atomic diameters. The geometry effect and most specifically the atomic size effect, is an important consideration in phase formation of metal alloys based on the classis Hume-Rothery rules of binary solid solution formation [25].

HEAs were first introduced having four core effects of high configurational entropy, lattice distortion, sluggish diffusion, and the cocktail effect [21,22]. High configurational entropy lowers the Gibbs free energy, stabilizing the solid solutions, specifically at high temperatures, and therefore reducing the probability of brittle secondary phases. The effect of configurational entropy on the solid solution stabilization at room temperature and lower temperatures have been challenged as mixing enthalpies due to chemical bonding and lattice strain can have equal or even more significant effect [21]. Lattice distortion is due to the differences between the atomic sizes

of the elements that are present in high concentration and with random distribution in the lattice of HEAs. The localized distortion in the HEA lattice, elastically interact with the movement of the dislocations resulting in solid solution strengthening [10,26]. Lattice distortion in HEAs has also been known to cause sluggish diffusion. It has been hypothesized that due to the fluctuation in potential energies of lattice sites in HEAs, the diffusing species will be trapped at local preferable bonding configurations, slowing the diffusion rate [10,27]. A schematic representation of the difference in potential energy profile in HEA lattice and pure element is shown in Figure 1. However, this has not been systematically studied and in some cases high diffusion rates have been observed in HEAs [10,27,28]. The cocktail effect first proposed by Ranganathan is not necessarily a core effect, but it means that we cannot expect the HEA to possess the linear superposition of the properties of its constituent elements [21,29].

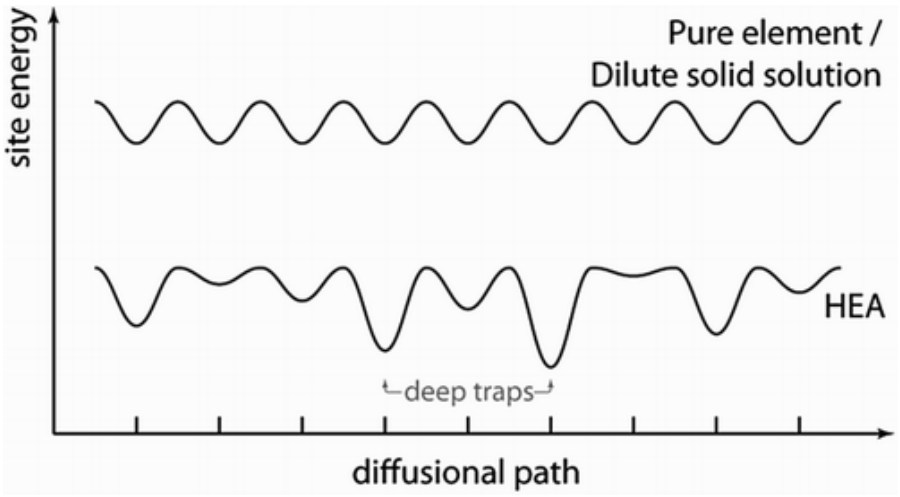

Figure 1. Schematic of the potential energy path in a pure element or a dilute solid solution and in HEA lattice. Deep energy traps can be observed in the HEA energy path [10,26]

Since the introduction of HEAs, development of non-equiatomic HEAs, multiphase HEAs, metastable HEAs, etc. has broadened the possible alloy design space even more in the search of alloys with preferable properties [30]. HEAs have been showing mechanical properties better than

or comparable to classical structural alloys, for instance nickel-based alloys and austenitic stainless steels, without any systematic endeavor to optimize the properties of HEAs through grain size refinement, fine tuning of phase fraction and other methods [1,5,8,10,14,19,20,30–33]. The room temperature tensile strength versus elongation to fracture for HEAs and other conventional structural alloys are shown in Figure 2.

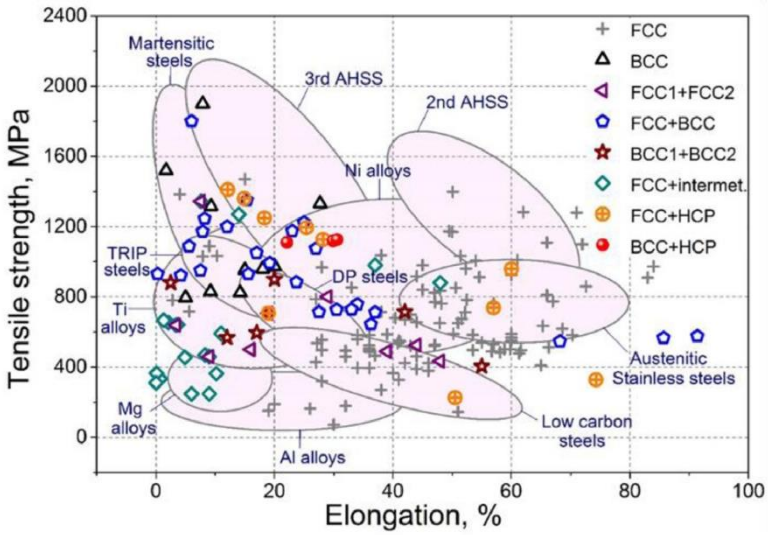

Figure 2. Tensile strength vs. elongation at room temperature for HEAs and conventional structural alloys [30].

As seen in Figure 2, HEAs have both high strength and high ductility compared to conventional metal alloys such as nickel alloys, austenitic stainless steels, and aluminum alloys. Single phase Face centered cubic (fcc) HEAs specifically is shown to have the highest strength and ductily due to not having brittle intermetallic phases and in the case of low stacking fault energy (SFE) fcc HEAs, the activation of deformation twins contributing to ductility of the alloy. Low SFE single-phase fcc HEAs have comparable properties to nickel-based superalloys and austenitic stainless steel typically having the same 3d transition metal elements, however, they have lower ultimate tensile strength compared to 2nd generation advanced high strength steels

unless they show twinning-induced plasticity (TWIP) effects [30]. The focus of this research is on single phase fcc HEAs due to their properties of high strength and ductility and in order to study slip and deformation twins which is observed in these alloys.

1.3 Plastic Deformation Mechanisms

When metals reach their yield point, they start to deform plastically. Depending on the composition and structure of the material and the environmental and loading conditions, different modes of plastic deformation can be activated and result in the plastic deformation.

The leading modes of plastic deformation in fcc metal alloys are full dislocation slip, partial dislocation motion (stacking fault), and deformation twinning. The activated mode depends on its corresponding effective energy barriers. The effective energy barriers depends on the grain orientation with respects to the external loading direction and the stacking fault energy of the alloy [34,35]. In a homogeneous material, dislocation slip and stacking fault or dislocation slip and deformation twin modes of deformation can coexist. However, due to similar Schmid factor, deformation twinning and stacking faults modes of plastic deformation cannot coexist [34].

Generalized stacking fault energy (γ-surface) is a measure of the energy difference between two adjacent planes on a given slip plane in a specific slip direction when shear deformation is occurring [36,37]. For instance, in the case of fcc crystal, the generalized stacking fault energy represents the sheared crystal energy dependency on the {111} plane along the $<11\bar{2}>$ direction [37]. The generalized stacking fault energy provides information on the alloy plastic deformation mechanisms [37,38]. The excess energy related to the stacking fault is called the intrinsic stacking fault energy γ_{isf}, the stacking fault energy determining the energy barrier to the produce of twin fault or stacking fault is called the unstable twinning fault energy and unstable stacking fault energy respectively [36,37]. Stacking fault energies are usually found through a combination of

density functional theory (DFT) calculations and X-ray diffraction (XRD) experiments. Deformation twinning is more probable in materials with low to medium SFE resulting in twinning induced plasticity (TWIP) [38] similar to TWIP steels behavior [39]. SFE of a couple of low to medium SFE HEAs are shown in Table 1.

Table 1. Shear modulus G, Poisson's ratio, lattice parameter and SFE of low to medium SFE HEAs [40].

Alloy	Shear Modulus G, (GPa)	Poisson's Ratio	Lattice Parameter ($\dot{A}$)	Stacking fault energy ($mJ.m^{-2}$)
CoCrNi	88±2	0.30±0.01	3.529±0.018	18±4
CoCrFeNi	85±2	0.29±0.01	3.565±0.014	27±4
CoCrFeMnNi	82±2	0.28±0.01	3.576±0.014	26.5±4.5

Dislocations are linear defects in the crystal lattice causing a lattice to undergo plastic deformation at lower stresses than what would have been needed for a perfect crystal lattice [41–43]. Due to the presence of dislocations, the crystal lattice atomic planes are able to slip by one atomic row at a time. Dislocation glide occurs when atomic layers shear relative to one another [44]. The slip system in crystal lattices consist of the plane on which the dislocation slips (slip planes) and the direction which the dislocation slips towards (slip direction) [45]. The slip plane is the plane with more atomic density and the closed pack of the slip plane is the slip direction. In the fcc crystal lattice structure, the {111} planes and the <110> directions are the slip systems [45]. In fcc metal alloys, the shortest lattice vectors and therefore the most probable Burgers vectors for dislocation slip are the ½<110> and <001> types. The 1/2<110> type is more energetically favorable and the <001> one is rarely observed [43,45–47]. The direction and magnitude of dislocation slip is represented by the Burgers vector. The Burgers vector for dislocation slip is along the lattice vectors and during the glide, the dislocations move from one lattice site to an adjacent one. The orientation of the slipped and unslipped regions within the crystal would not

change [48]. For slip to occur the critical resolved shear stress for slip must be achieved. Therefore, the knowledge of the critical resolved shear stress is an important consideration for designing and understanding plasticity in polycrystalline alloys. Critical resolved shear stress will be explained in section 1.4.

Twinning is another mode of plastic deformation which is widely seen in alloys with body centered cubic (bcc) and hexagonal closed pack (hcp) and fcc lattice structures. Experiments on single crystals have shown that deformation twinning occurs at low strength and even before yield in bcc metal alloys. In fcc alloys, it is often delayed until later in the plastic region [48,49]. Deformation twinning usually is limited to the low to medium stacking fault energy alloys in the case of fcc. In these alloys the deformation twinning is very sensitive to temperature, strain, and strain rate and its probability increases with decrease in temperature and increase in strain and strain rate [48–50].

Homogeneous simple shear of the parent lattice forms a twin and therefore coordinated individual atom displacement occurs (Figure 3). Twin and the parent lattices are related by reflection in some plane and in contrary to slip the twinned and untwinned parts of the crystal do not have the same crystallographic orientation [48,49]. In the case of defect-assisted twin nucleation, dislocation configurations dissociate into single or multi-layered stacking fault serving as the twin nucleus.

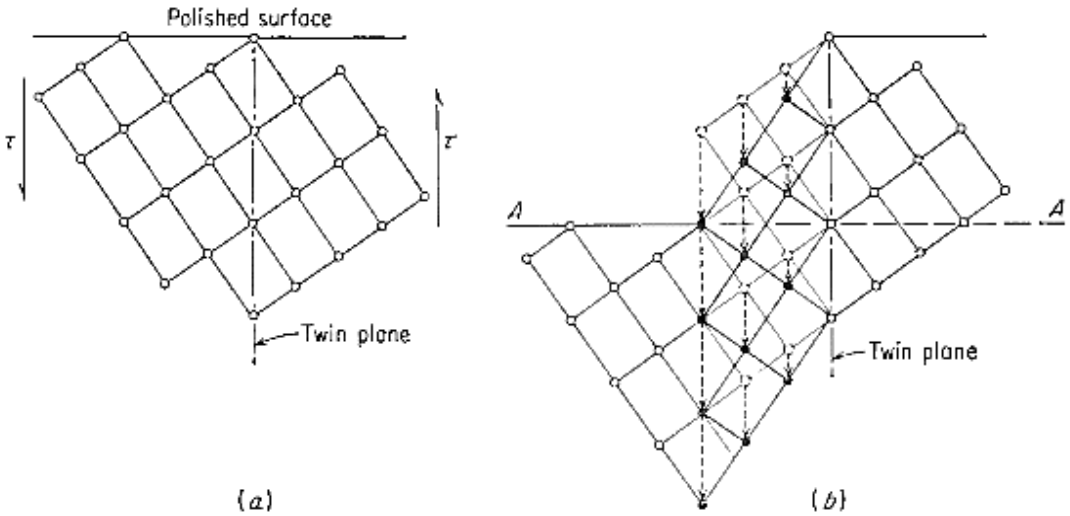

Figure 3. Picture of twinning illustrating the atoms and the crystal orientation change with respect to the twin plane. (a) is showing the unchanged crystal and (b) is showing the twinned crystal [45].

In fcc metals, twinning begins when slip is activated on at least two slip systems. The reaction of the primary system dislocations with Burgers vectors, and the coplanar system dislocations with Burgers vectors form three Shockley partials [51]. These Shockley partials rearrange on successive planes and three-layer fault is formed. Then with the growth of the three-layer faults in a slip band, a twin is obtained. This theory has been experimentally observed and the overall described reaction is energetically favorable [48,49,52]. In fcc metal alloys the twin planes are the {111} and the twin directions are the <112> direction [49,52]. The stress needed for twin nucleation is called the critical resolved shear stress for twinning and it is further explained in Section 1.4 [53,54]. Twins observed in transmission electron microscopy (TEM) micrographs for $Al_{0.1}$CoCrFeNi and electron back scatter diffraction (EBSD) inverse pole figure (IPF) map for $Al_{0.5}$CoCrFeNi HEA are shown in Figure 4.

(a) 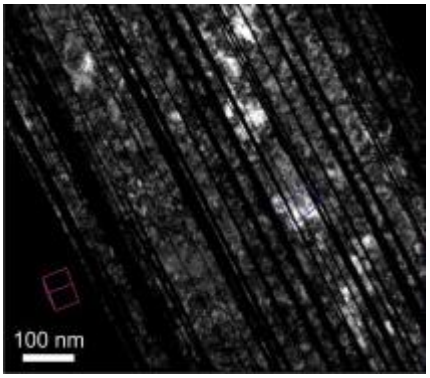

(b) 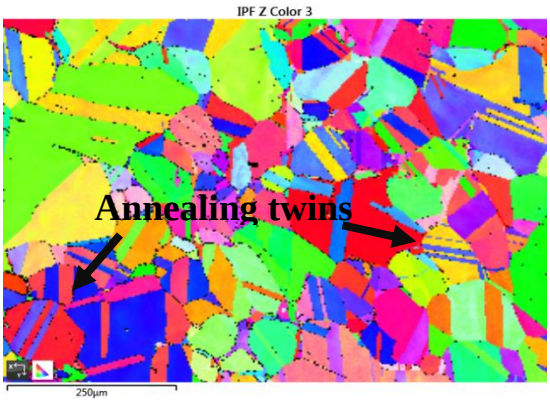

Figure 4. Deformation twins of $Al_{0.1}CoCrFeNi$ in a TEM micrograph on the (a) (Source: [53]) and annealing twins of $Al_{0.3}CoCrFeNi$ in an IPF map using EBSD (b).

There are different factors affecting the nucleation and growth of deformation nanotwins in low stacking fault energy fcc metals and metal alloys. Among these factors are temperature, grain size, composition and stacking fault energy, strain rate, and strain. Studies have shown that the lower and closer to the cryogenic temperatures, it is more favorable for the twins to nucleate and grow [12,20,54,55]. The grain size has an effect on the yield strength of the alloy considering the Hall-Petch. The smaller the grain size the higher the yield of the alloy and therefore the stress needed to activate the twins would be achieved earlier in the plastic deformation stage. The Hall-Petch equation is shown below [56]:

$$\sigma_y = \sigma_0 + k\frac{1}{\sqrt{D}} \qquad (4)$$

where σ_0 and k are constants dependent on chemistry and microstructure, D is the grain size, and σ_y is the yield strength. This equation stems from the empirical work of Hall and Petch on low carbon steels [57,58]. On the other hand, it has been shown that that grain size decrease, increases the twin spacing and decreases the twins' thickness and therefore decrease the twinning activity. Therefore, an optimized grain size is needed to have deformation twins nucleating and becoming activated [38,53,59]. It is worth mentioning that main influence of twinning is improving the work-

hardening rate and that is due to the grain being divided to twinned and untwined regions, similar to grain refinement, causing dynamic Hall-Petch effect and delaying the local necking [60,61]. Stacking fault energy (SFE) plays a role on the possibility of deformation twin nucleation and growth. Stacking fault energy depends on composition and temperature and plays an important role in the alloy deformation mechanisms [60,62,63]. Depending on the SFE the deformation mechanisms activated for instance for the case of fcc metals can be slip, twin, phase transformation or a combination of these mechanisms [60]. SFE is an indication of the Shockley partial dislocations distance and the possibility of local stacking faults to form [60].

The range of SFE to have each deformation mechanisms is shown in Figure 5 [64]. Tunning the stacking fault energy is considered a design strategy for metal alloys to control the activation of deformation mechanisms. For instance in designing twinning-induced plasticity (TWIP), transformation-induced TRIP and TWIP/TRIP austenitic steels, HEAs, and other metal alloys, tuning the SFE by changing the composition has been widely used [59,64].

Strain-rate and strain also have an effect on the twin nucleation and growth in HEAs. Twinning has been widely observed in tension at cryogenic temperature, but it has been observed that at room temperature twinning is not activated in CoCrFeNi and CoCrFeMnNi in quasi-static tension. But when the strain-rate is in the dynamic range there is an addition of deformation twins [19]. Also, at the quasi-static strain-rates at high strain of more than 20% deformation twins have been observed [54].

Computational studies have also been done on twin nucleation and growth in fcc metals in a smaller scale [34,65]. Twinning in metastable HEA $Fe_{80-x}Mn_xCo_{10}Cr_{10}$ and CrMnFeCoNi was studied based on the effective energy barriers and the first-principle theory and it was found that the main mode of deformation in face-centered cubic metastable high entropy alloys and it depends

on the shear strain [34]. In CoCrFeMnNi the critical resolved shear stress for twinning of CoCrFeMnNi has been found to be 235±10 MPa [66].

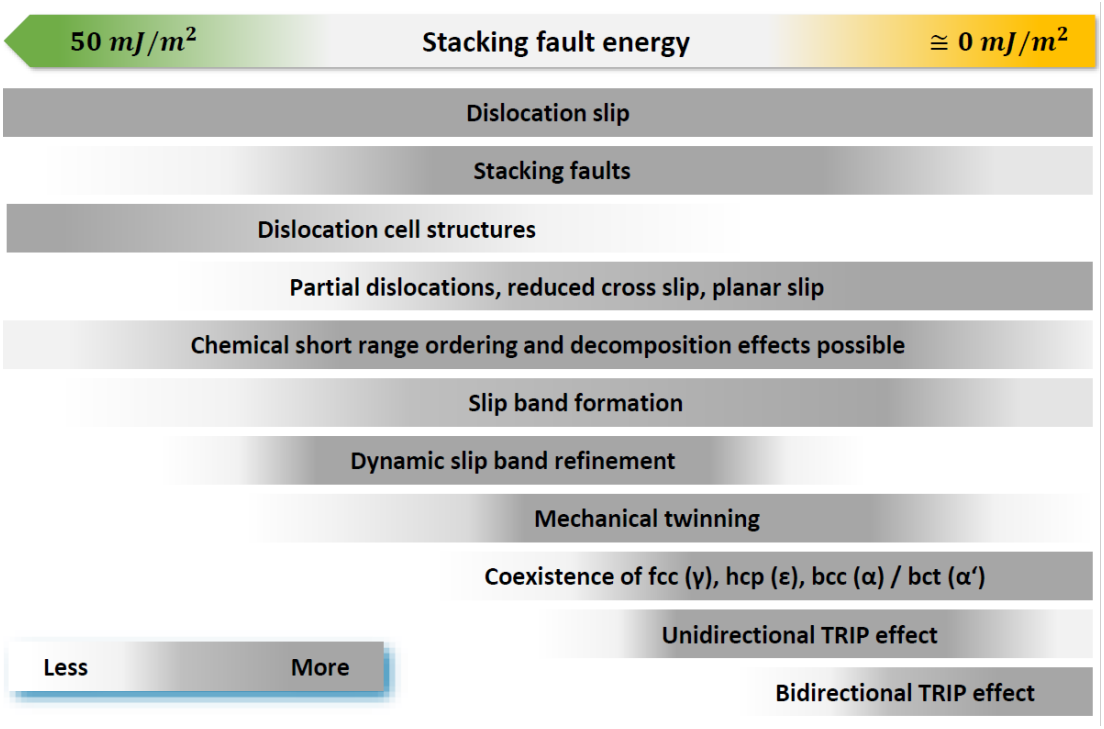

Figure 5. Effect of stacking fault energy on the activation of deformation mechanisms in metal alloys [64]

The effect of GB orientation on deformation twinning in TWIP steels and copper and aluminum having fcc crystal structures have been studied to some extend [67,68]. But the effect of GB characteristics and specifically in HEAs has not been studied thoroughly and the existing studies are preliminary [69,70]. The overview of the factors affecting twin and nucleation growth in HEAs and the corresponding literature for each factor is shown in Figure 6.

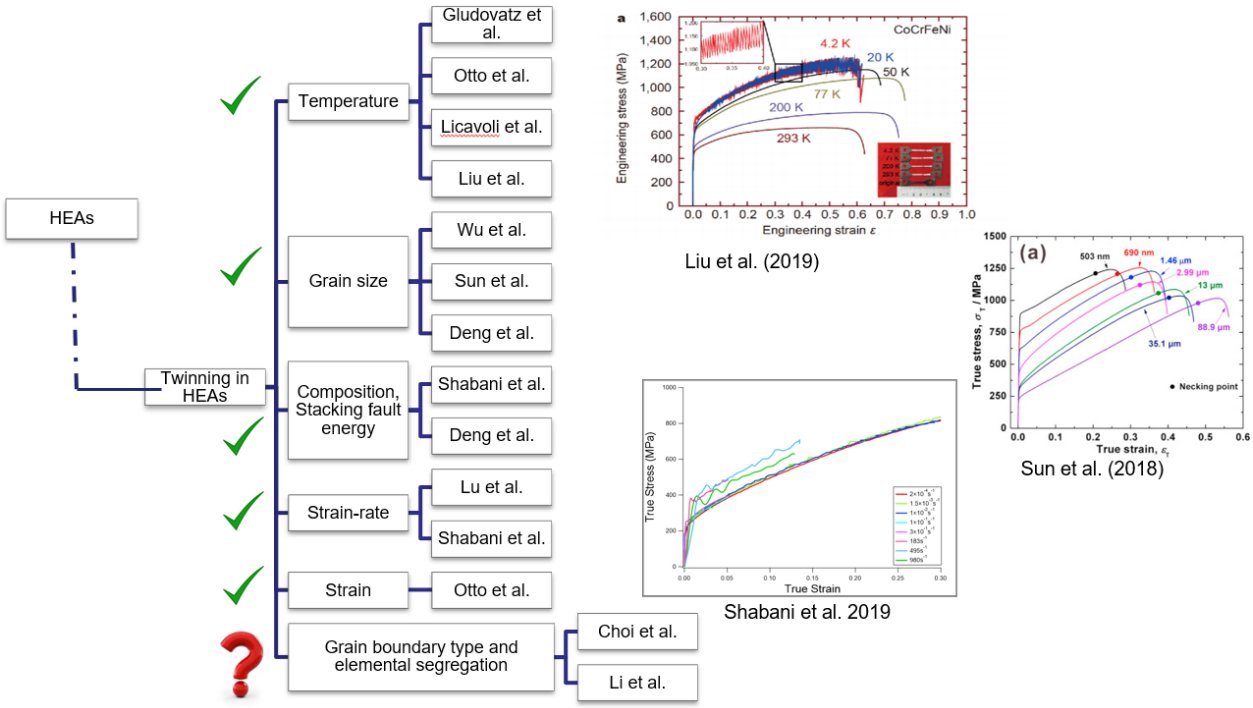

Figure 6. Factors effecting the twin nucleation in fcc HEAs and the corresponding selected literature.

1.4 Critical Resolved Shear Stress

As mentioned in the previous section, fcc lattice structures have slip systems which are planes and directions at which dislocation slip occurs. Fcc lattice structure have 12 slip systems consisting of the combination of four octahedral planes in the {111} family and six <110> directions. The 12 possible slip systems are shown in Table 2.

Table 2. The planes and slip directions of the fcc 12 slip systems.

	Plane	Slip Direction
1	(1 1 1)	[-1 0 1]
2	(1 1 1)	[1 -1 0]
3	(1 1 1)	[0 -1 1]
4	(1 -1 1)	[0 -1 -1]
5	(1 -1 1)	[-1 0 1]
6	(1 -1 1)	[-1 -1 0]
7	(-1 1 1)	[-1 0 -1]
8	(-1 1 1)	[-1 -1 0]
9	(-1 1 1)	[0 -1 1]
10	(-1 -1 1)	[0 -1 -1]
11	(-1 -1 1)	[-1 0 -1]
12	(-1 -1 1)	[1 -1 0]

When a crystal is under loading the shear stress resolved on the slip plane in the slip direction for each of the slip systems is called the resolved shear stress. The resolved shear stress can be found by using the equation below:

$$\tau = \sigma cos\phi cos\lambda \qquad (5)$$

where τ is the resolved shear stress on the slip plane in the slip direction, σ is the tensile stress on the crystal, ϕ is the angle between the load axis and the slip plane normal, and λ is the angle between the load axis and the slip direction. A schematic of the crystal slip plane, normal to the slip plane, slip direction and the external tensile force is shown in Figure 7. The term $cos\phi cos\lambda$ is called the Schmid factor, M. If σ would be replaced with the minimum stress needed to activate the slip, then critical resolved shear stress, τ_{crss} is found. For every crystal based on its orientation with respect to the loading direction, Schmid factors for each of the slip systems can be found. The slip system with the maximum Schmid factor, considering that other factors of the experiment are unchanged, will be the most probable slip system for slip to start nucleation on.

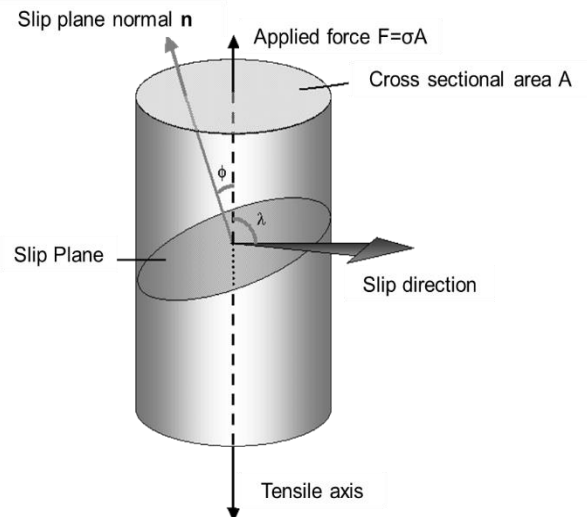

Figure 7. Schematic of a crystal and its slip plane and slip direction with respect to the external tensile load.

The same description of the resolved shear stress and the critical resolved shear stress can be described for deformation twins and based on the twin planes and directions. Fcc lattice structures also have 12 twin systems consisting of the combination of four octahedral planes in the {111} family and six <112> directions. The possible twin systems in fcc crystals are shown in Table 3 as well as in Figure 8 using a Thompson tetrahedron [71].

Table 3. The planes and twin directions of the fcc 12 twin systems.

	Plane	Twin direction
1	(1 1 1)	[1 1 -2]
2	(1 1 1)	[1 -2 1]
3	(1 1 1)	[-2 1 1]
4	(1 -1 1)	[1 -1 -2]
5	(1 -1 1)	[1 2 1]
6	(1 -1 1)	[-2 -1 1]
7	(-1 1 1)	[-1 1 -2]
8	(-1 1 1)	[-1 -2 1]
9	(-1 1 1)	[2 1 1]
10	(-1 -1 1)	[-1 -1 -2]
11	(-1 -1 1)	[-1 2 1]
12	(-1 -1 1)	[2 -1 1]

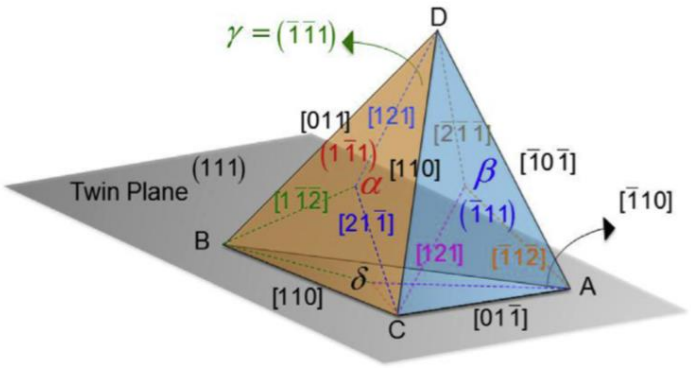

Figure 8. Possible twin systems in an fcc crystal using the Thompson tetrahedron [71].

1.5 Scientific Contributions

HEAs having interesting properties are great candidates to be used as structural materials in extreme environment applications. Due to the unique composition of HEAs compared to conventional metal alloys, having different elements in their lattices, there exists local fluctuations of composition, stacking faults energy, lattice distortion, and lattice strain [21]. Plastic deformation mechanisms in low stacking fault fcc HEAs are dislocation slip and deformation twin. Due to the unique composition of HEAs, factors influencing the plastic deformation mechanisms need to be thoroughly studied.

This research will address the following research questions:

a) What is the critical resolved shear stress for dislocation slip in $Al_{0.3}CoCrFeNi$?

b) Does GB type influence the twin nucleation in fcc HEAs?

c) What is the critical resolved shear stress for twin nucleation in CoCrFeNi? Does GB type and temperature influence it?

d) Does elemental segregation at GBs influence the twin nucleation for different GB types?

The main scientific continuation of this research are as follows:

a) Slip critical resolved shear stress in an fcc low stacking fault energy HEA was found experimentally using high resolution digital image correlation and electron backscatter diffraction,

b) Grain boundaries have been experimentally observed to be sites for deformation twin nucleation in HEAs. However, the effect of different grain boundaries on the twin nucleation in HEAs and other low stacking fault energy fcc metal alloys has not been thoroughly studied. In this study the effect of different symmetric twist grain boundaries on the twin nucleation and the mechanical properties of HEAs at cryogenic temperatures was found using molecular dynamics modeling.

c) Local chemical fluctuations in HEAs can result in elemental segregation at sites of the lattice. Grain boundaries are planar defects that cannot be considered as scalar objects having homogeneity. Therefore, grain boundaries are possible sites of elemental segregation in HEAs. Elemental segregation at grain boundaries and its effect on twin nucleation and growth in fcc low stacking fault energy HEA was found at three different temperature 77 K, 100 K, and 300 K.

This research provides insight into the plastic deformation mechanisms in fcc low stacking fault energy high entropy alloys. Experimentally the critical resolved shear stress in $Al_{0.3}$CoCrFeNi HEA is found for the first time under tension at room temperature. The effect of grain boundaries' geometry and elemental segregation on the deformation twin nucleation has not been thoroughly studied in HEAs and in general in other metal alloys. Computationally using CoCrFeNi HEA bicrystal models the preferential grain boundaries (GBs) for twin, GB elemental segregation and its effect on twin nucleation, at three different temperature of 77 K, 300 K, and 600 K is found.

The results of this research provide the essential information for GB engineering and segregation engineering in HEAs to increase their twinnability. Based on the outcomes from this study, alloys can be designed with increased boundaries preferential for twin nucleation and further improve the properties of HEAs and metal alloys.

1.6 Chapters Overview

Chapter two includes the introduction to the experimental techniques for the study to find the slip critical resolved shear stress in the fcc $Al_{0.3}$CoCrFeNi HEA under tension using the strain map from high resolution digital image correlation and the microstructural map from the electron backscatter diffraction. Chapter three presents the background and motivation, methodology, results, discussion, and conclusions on the experimental study. Chapter four goes through the introduction to the computational methodologies used in this research for the study to find the effect of different symmetric twist grain boundaries in CoCrFeNi bicrystals and the GB elemental segregation on the mechanical behavior and twin nucleation at three different temperatures 77 K, 300 K, and 600 K. Chapters five and six go through background and motivation, methodology, results and discussion, and conclusion on the mechanical behavior, material properties and deformation mechanisms in the CoCrFeNi bicrysals with different grain boundaries. Chapter seven covers the overall conclusions from this study, summary, and future work and Chapter eight contains the list of references used in this study.

CHAPTER TWO: INTRODUCTION TO THE EXPERIMENTAL TECHNIQUES

Parts of this section has been used as part of a journal paper.

An experimental approach was used to address the first objectives of this research in which mechanical tensile testing, high resolution image correlation, and electron microscopy were used to study the tensile behavior and calculate the slip critical resolved shear stress in $Al_{0.3}CoCrFeNi$ polycrystals. In this chapter the experimental techniques used are discussed and in the following chapter the experimental research including, background and motivation, materials and methods, results and discussion, and conclusions are presented.

2.1 Digital Image Correlation

Digital image correlation (DIC) is a non-contact optical method for acquiring the displacement fields during mechanical testing. In this technique, the region of interest on the sample is speckled to produce a randomized speckle pattern. The technique and materials used to create the speckle patterns depend on the specimen material, testing condition, and the resolution at which the strain heterogeneity is expected to be acquired. The DIC pattern size has an optimum feature size of 3-5 pixels [72]. The variation and density of the speckle pattern should provide unique subsets in different regions with the same amount of black and white regions with good contrast. Also, the applied pattern should be thin relative to the test specimen, and the bonding between the test piece and the applied pattern should be good. The applied pattern should also have acceptable fidelity and deform conformally with the sample surface [73]. In this research three different powders, aluminum oxide 1000 mesh, aluminum oxide 360 mesh, and silicon carbide 1200 mesh were tested to create the speckle pattern. All of the three mentioned powders showed acceptable bonding with the surface of the specimen. However, the 1200 mesh silicon carbide powder provided better contrast and resolution. To have sufficient contrast between the lightest

and the darkest regions of the pattern the light intensity on the region of interest is of importance [73]. During the mechanical testing multiple concurrent images are taken of the area of interest. A camera and light setup to use DIC for a tensile mechanical test is shown in Figure 9.

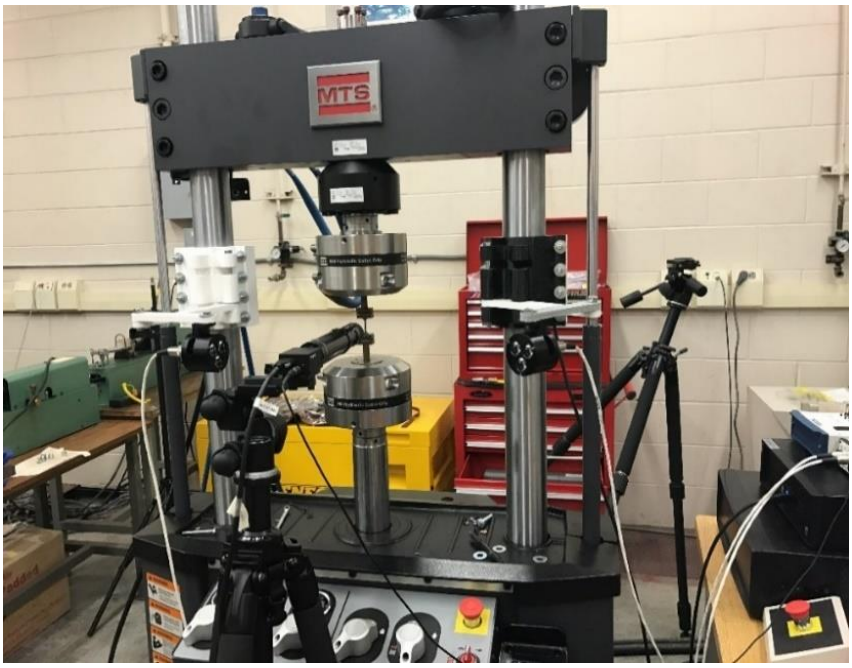

Figure 9. Camera and light setup to use DIC for a tensile mechanical

Once the images have been acquired, commercial DIC packages for instance VIC-2D from Correlation Solutions, Inc., independently developed DIC code, or in-house image correlation codes can be used to process them. DIC tracks the motion of a set of points on a reference image in a Lagrangian sense within subsets of the defined area of interest [73]. The reference image can be chosen to be the initial image taken prior to the start of the test, or incremental correlation can be used so that each image is correlated to its previous image [73,74]. The incremental correlation is usually used when there are the images change significantly during the test and cannot be correlated to the initial image. The pattern in each of the subsets of the image is approximated using interpolant function which is then allowed to change from the reference image based on the

subset polynomial shape function [73]. The correlation algorithms can be based on the differential methods using the first order Taylor's series expansion or they can be based on the template matching which uses the minimization of the gray value different between the subsets in the deformed images and the reference image [75]. Then each of the subsets of the deformed images are matched with a subset of the reference image.

Through the coordinates change of the measurement points within each subset the displacements are found across the whole area of interest. A strain shape function is fit to the displacements resulting in an analytical description of the displacement field. Using the spatial derivatives of the displacements in each direction, the strain tensor components are calculated for each of the subsets and the strain map is acquired.

2.2 Electron Microscopy

Microscopes are widely used in material characterization. In an attempt to increase the resolution of microscopes, electron microscopes were developed. Resolution power of microscopes, which is the minimum distance between to neighboring object points that can be separately images, is one of the most important aspects of a microscope. The resolution of a light microscope is limited to the wavelength of the visible light. With the development and improvement of electron microscopes higher resolutions have been achieved from the resolutions of micrometers achieved with optical microscopes to resolution of picometers achieved by scanning tunneling microscopes and transmission electron microscopes [76–79].

In general electron microscopy techniques can be divided into two broad techniques, scanning electron microscopy (SEM) and transmission electron microscopy (TEM). Using SEM lower resolutions are achieved compare to TEM but surface image of bulk samples with larger

depth of focus can be achieved [76–79]. Depending on the goal of the study and resolution of the features being studied, one or multiple microscopy techniques can be used.

SEM is the most used microscopic technique due to the ease of specimen preparation, general simplicity of the interpretation of the images, and the user-friendliness of the apparatus compared to other techniques. Chemical analysis of different elements is also achievable by SEM [76]. SEM is widely used in materials science to acquire microscopic structure and differentiating several phases from each other due to great depth of field and lateral resolution [79]. In the scanning electron microscope, the focused electron beam scans the surface of the specimen line by line and based on the interaction between the electron beam and the sample, signals are formed which are then electronically detected and amplified [76,77,79]. The inelastic interaction between the primary beam electrons and the specimen atoms atomic shells is illustrated in Figure 10.

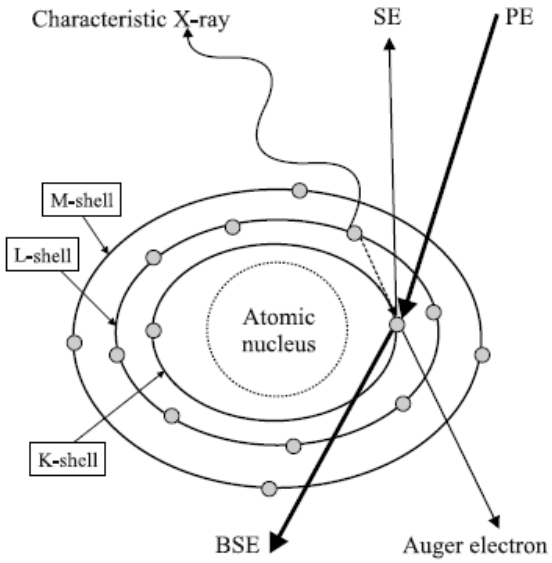

Figure 10. Inelastic interaction between the primary beam electrons and the specimen atoms atomic shell electrons [79].

When the incident electrons shown as PE in Figure 10 have enough energy, the valance electrons of the surface atoms are released from the atomic shell, which are called the secondary

electrons. The secondary electrons are used to have the signal and eventually a micrograph of a thin layer of the surface is created [76]. After the surface atom valance electrons are released due to the interaction with the incident electrons, the resulted empty electron valance is filled again by the relaxed atom. Secondary effects as a result of the excess energy release of the electron occurs which varies depending on the vacant electron state which are the emission of photon, Auger electrons, visible wavelength photons, and X-ray photons [79]. Each of these secondary effects contain information from either the sample's surface microstructure, morphology, phase and chemical composition.

Using the X-ray emission as a secondary effect of the interaction between the incident beam and the specimen surface electron in an SEM, compositional analysis of the elements of the sample surface is possible [80,81]. Energy-dispersive X-ray analysis (EDX) is a technique in which the electron beam is moved across the material, and by analyzing the energy of the emitted X-rays an image of the elements in the specimen can be formed as the energy of emitted X-rays are element specific [81]. It is noteworthy that the emitted X-rays are from a region about 2 micrometers deep from the sample surface. Therefore EDX is not considered as a true surface technique [80].

Electron backscatter diffraction (EBSD) based on SEM is another powerful technique that can be used to quantitatively measure the microstructural information of the sample surface such as the texture, grain size, point to point orientations and phase identification [82,83]. Moreover, the boundary misorientations and the distribution of boundary types can be extracted from EBSD data [84]. When the incident beam hits the sample surface, a fraction of the electrons diffracts with a small loss of energy. Some of these electrons are at the atomic planes with angles that satisfy the Bragg equation [85]:

$$n\lambda = 2dsin\theta \qquad (6)$$

where n is an integer, d is the diffracting plane spacing, θ is the angle of incidence of the electrons on the diffracting plane, and λ is the electrons wavelength. The image produced on the phosphor screen from these diffracted electrons, form characteristic Kikuchi bands [85]. Then a sensitive charged-couple device (CCD) camera is used to acquire the images which are then postprocessed by pattern averaging and background subtraction as seen in the schematic in Figure 11 to produce the EBSD microstructural data and maps [84].

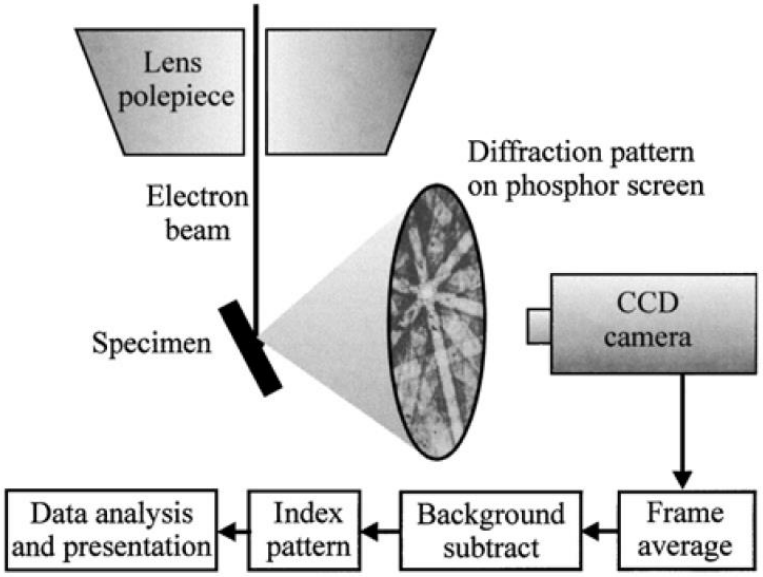

Figure 11. Schematic of the components and process to acquire EBSD data in SEM [84].

When carrying out EBSD, the sample is tilted between 60º and 70º from the horizontal to optimize the diffraction pattern and the scattered electrons fraction [82,84–86]. Data from EBSD along with the data from EDS can be used for phase characterization of the specimen surface [82,84,86].

2.3 Summary

In this chapter the fundamentals of the experimental methods used in this research has been covered. In the following chapter, the experimental study of the slip critical resolved shear stress in $Al_{0.3}$CoCrFeNi HEA using the techniques described in this chapter is explained. Specific material and methods of the research are explained in the next chapter.

CHAPTER THREE: CRITICAL RESOLVED SHEAR STRESS FOR SLIP IN $AL_{0.3}$COCRFENI HIGH ENTROPY ALLOY

Parts of this section has been used as part of a journal paper.

In this chapter the experimental study of the critical resolved shear stress for slip in fcc low stacking fault energy $Al_{0.3}$CoCrFeNi HEA is described containing the background and motivation of the study, the specific materials and methods, results and discussion, and the conclusions.

3.1 Background and Motivation

HEAs were first introduced with the idea of achieving single phase metal alloys or with minimal secondary phases by decreasing the Gibbs free energy through increasing the entropy of formation. Therefore, initially the idea was to develop alloys with multiple main elements in equimolar proportions to achieve highest entropies. Later, this approach was relaxed and HEAs were alloyed with elements in different proportions to achieve improved properties [64,87]. Adding aluminum at different concentrations Al_x to CoCrFeNi has been investigated and it reduced the density of the alloy and increased the yield strength due to the solid solution strengthening effect [15,18,88–94]. Depending on the amount of aluminum concentration in Al_xCoCrFeNi HEA the alloy can be single phase fcc for Al contents of less than 5 at%, combination of fcc and bcc phases for Al contents of between 5 and 9 at% and bcc phase for Al contents of more than 9 at% [95–97]. The EBSD IPF and EDS maps of $Al_{0.3}$CoCrFeNi being a single phase fcc alloy and $Al_{0.5}$CoCrFeNi having both fcc and bcc phased are shown in Figure 12.

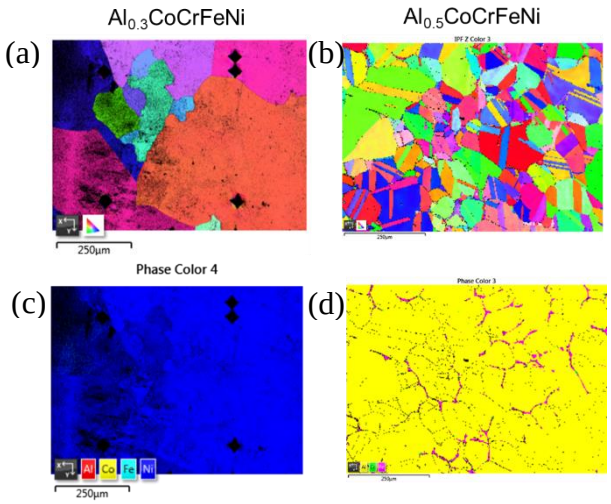

Figure 12. EBSD IPF maps (a), (b) and EDS maps (c), (d) of $Al_{0.3}CoCrFeNi$ and $Al_{0.5}CoCrFeNi$ HEAs being single phase fcc and having fcc and bcc phases respectively.

$Al_{0.3}CoCrFeNi$ HEA is a single phase fcc HEA with desirable properties such as high strength, corrosion resistance, and fatigue resistance [92,94]. In fcc metals and metal alloys, the dominant mode of plastic deformation is slip dislocation on {111}<110> system with Burgers vector of $|b| = \frac{\sqrt{2}}{a_0}$, a_0 being the lattice constant [98].

Slip nucleation and slip CRSS has been studied in some 3d transition HEA single crystals at cryogenic and room temperature. Slip nucleation has been studied in the $[5\bar{9}1]$ oriented single crystal CoCrFeMnNi, a single phase fcc HEA, and the tensile CRSS was found to be 175 MPa at 77 K [98]. CRSS for slip was found to be temperature dependent in single crystal Cantor alloy regardless of orientation, 56 MPa and 153 MPa at 293 K and 77 K respectively [99]. Cantor alloy bulk room temperature Slip CRSS has also been found by single crystal micropillar compression to be 33-43 MPa [100]. However, the CRSS for slip has not been found for $Al_{0.3}CoCrFeNi$ HEA. Grain level and sub grain level deformation mechanisms and the factors influencing them are essential information in design and development of improved HEAs and metal alloys in general.

The micro- and nano-scale mechanisms' information such as the slip CRSS can provide information to develop physics based models of the HEAs.

In this experimental study the single phase fcc $Al_{0.3}CoCrFeNi$ polycrystal was manufactured using vacuum induction melting. Quasi-static strain rate tensile tests were run on flat dog-bone samples at room temperature. Strain was measured using high resolution digital image correlation (HRDIC) during the tensile test. Critical resolved shear stress for slip was found by overlaying the strain map from HRDIC and the microstructural data from EBSD providing an insight on the deformation mechanisms in these alloys.

3.2 Materials and Methods

In the previous chapter background and overview of the experimental methodologies were explained. In this section the specific methodology used for the experimental study of slip critical resolved shear stress in $Al_{0.3}CoCrFeNi$ HEAs are explained.

$Al_{0.3}CoCrFeNi$ samples were manufactured by vacuum induction melting method. Then they were cold rolled to 60% and annealed for 1 hour at 1200°C. Using electro-discharge machining, tensile test specimens in the shape of flat dog-bones with gauge length of 16.5 mm, width of 3 mm, and thickness of 2 mm were made. One side of the sample was grinded and polished using the Buehler EcoMet™ 3 grinder-polisher. This was done in incremental steps up to P4000. The specimen was further polished using diamond pastes with abrasive size down to 0.05 microns then vibro-polished for 10 hours.

Five Vickers indentation markers were used to mark the area of interest. The Vickers markers were used to overlay the strain heterogeneity map from high resolution digital image correlation to the microstructural information from EBSD. The four Vickers markers marked the

rectangular area of interest of 450 µm × 400 µm and the fifth one was for the alignment consideration [101].

Before and after the tensile test, EBSD was performed on the area of interested in order to acquire microstructural map. Hitachi SU6600 SEM was used along with the aZtecHKL EBSD system software from Oxford instruments to acquire the microstructural data. A 45° tilted holder was used to attach the sample using double side conductive carbon tape. The microscope stage was then tilted for 25° to achieve the total angle of 70° between the sample surface and the beam needed to acquire EBSD data. The accelerating voltage used was 20.0 kV, the acquisition speed was 67 Hz, and the step size was 4 µm. The EBSD data from the area of interest, polished as described before, prior to and after the mechanical testing was used to be postprocessed using MTEX.

The polished surface of the sample was powdered speckled for the purpose of HRDIC using silicon carbide powder grit 1200 mesh having the particle size of 3.8 µm. The fine powder particles were air blasted on the specimen surface. The area of interest marked with the Vickers markers and powder speckled is shown in Figure 13 taken under a light microscope.

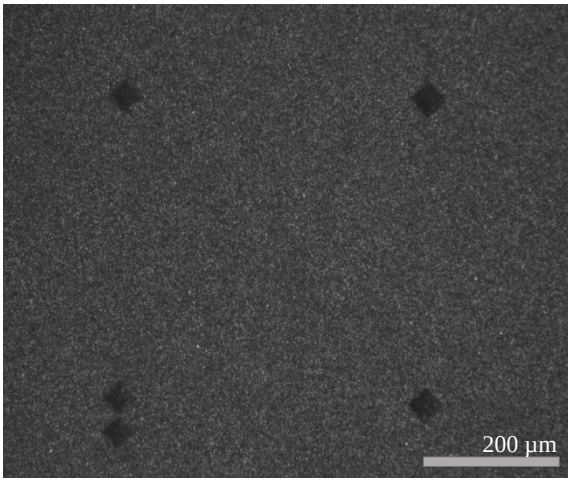

Figure 13. The area of interest in the middle of the flat dog-bone gauge for the $Al_{0.3}$CoCrFeNi sample speckled pattern and marked using five Vickers markers (black diamonds).

To run the tensile test at room temperature a Psylotech 10 kN load horizontal load frame and the Psylotest controlling software were used. The test profile created in the Psylotest was made by a combination of ramp profiles and pauses in between. The displacement-controlled ramp profiles had the velocity of $3.2 \times 10^{-3}\ {}^{mm}/_{s}$ accommodating the tensile test quasi-static strain rate of $2 \times 10^{-4}\ {}^{1}/_{s}$. The ramps durations were 5 minutes. After each ramp profile pauses of 30 seconds were used during which the camera was refocused if needed. Due to the high resolution of the test, the images went out of focus during the test and therefore could not be used for DIC purposes if the pauses for refocusing the images were not added. The frequency of data acquisition was 20 Hz. An Olympus optical microscope was used with the 20x magnification lens with corresponding resolution of 0.34 microns/pixel. The Point Grey GS2 camera is attached to the microscope for taking the pictures using the Vic-Snap software as the test is running. The images taken during the test need to be in focus and with the 20x magnification this is hard to accomplish as the external noise and vibrations would cause the images to go out of focus. Therefore, the whole setup was placed on an isolation table pressurized at 80 psi to reduce noise and vibration from the ground. The uniaxial tensile tests were performed at room temperature. The setup is shown in Figure 14.

The load data acquired from the Psylotest output file were used to find the engineering stress by dividing to the initial cross-sectional area of the gauge of the sample as described by the following equation:

$$\sigma_{eng} = \frac{F}{A_i} \qquad (7)$$

where σ_{eng} is the engineering stress, F is the applied load, and A_i is the initial cross-sectional area of the sample gauge.

The DIC analysis was done using Correlated Solutions software, Vic-2D with a subset size of 51 pixels and step size of 5 pixels. The gray value interpolation was selected to be 8-tap spline interpolation and Gaussian weights were considered for the subsets. The resolution error measurements were found to be 15 με by averaging the strain of the area of interest found from five images taken prior to the start of the test at zero load. Using the strain from HRDIC averaged on the area which the HRDIC post-processing have been applied to, and the stress found from the load output, the engineering stress-strain curve was plot and the material properties were extracted.

The microstructural information from EBSD and the full field strain map from HRDIC were overlaid using the five Vickers indentation markers as explained by Pataky et al. [101]. The Schmid factors for each of the grains were found using MTEX and the MATLAB code generated for postprocessing the EBSD data. The activated slip system and its corresponding Schmid factor is found. Then using the stress initiating the dislocation slip the critical resolved shear stress for dislocation slip activation was found.

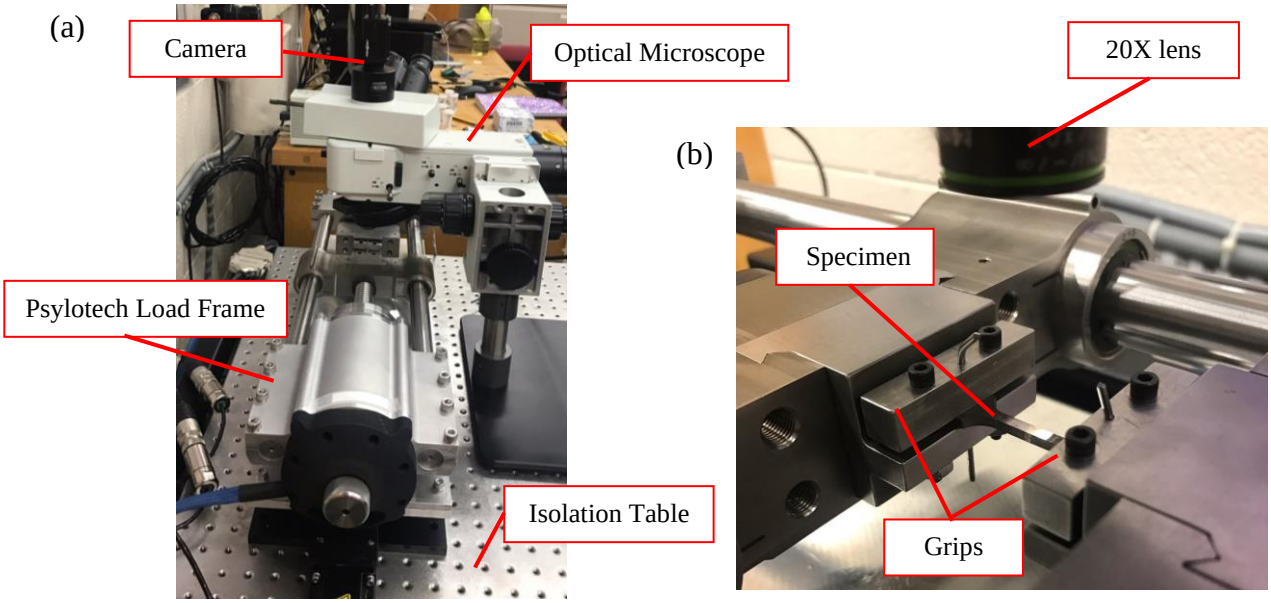

Figure 14. The mechanical testing and digital image correlation setup on an isolation table. (a) Whole setup including the Psylotech load frame, Olympus optical microscope with a 20X lens, a Point Grey camera connected to a computer for data acquisition. (b) Close up of where the sample is set up in the Psylotech grips.

3.3 Results and Discussion

Microstructure

The initial microstructure of the area of interest marked by the Vickers indentation markers is presented in Figure 15. The figure includes the SEM micrograph, energy EDS elemental maps, and the EBSD IPF Z map. The grain that is used for slip tracing is shown in Figure 15 (a) enclosed by dashed black lines. The possible slip systems with the corresponding Schmid factors found using the Euler angles for this grain are shown in Table 4. The slip systems with the highest Schmid factors are specifically of interest as they will be used for slip tracing and finding the slip CRSS.

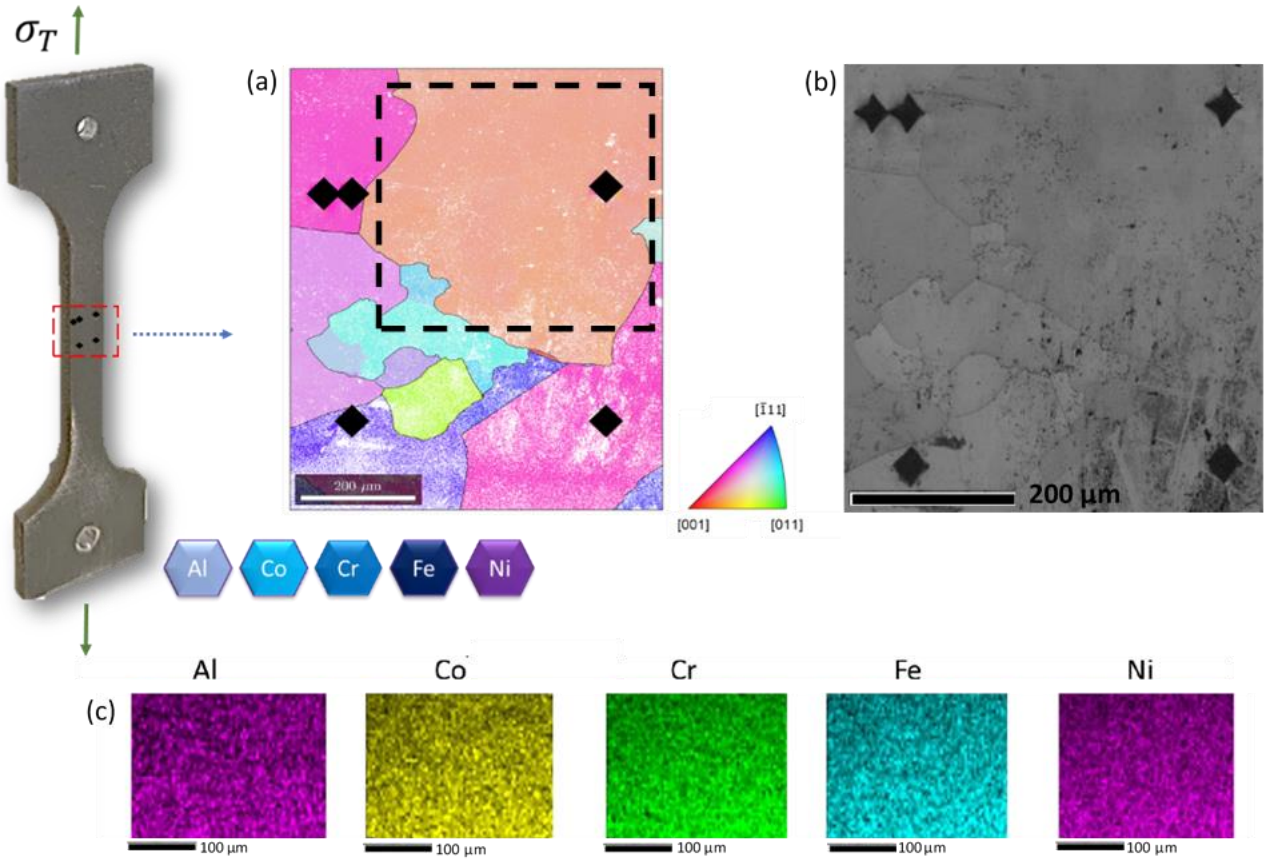

Figure 15. $Al_{0.3}CoCrFeNi$ microstructure. (a) EBSD IPF Z map using SEM denoting the grain orientation, (b) SEM micrograph, (c) EDS elemental map. The black diamonds are the Vickers indentation markers.

Table 4. Slip systems and the corresponding Schmid factors of the grain of interest. Slip systems with maximum Schmid factors are colored in the table.

Plane	Slip Direction	Schmid Factors
(1 1 1)	[-1 0 1]	-0.317
(1 1 1)	[1 -1 0]	0.082
(1 1 1)	[0 -1 1]	-0.082
(1 -1 1)	[0 -1 -1]	-0.083
(1 -1 1)	[-1 0 1]	0.083
(1 -1 1)	[-1 -1 0]	-0.318
(-1 1 1)	[-1 0 -1]	0.318
(-1 1 1)	[-1 -1 0]	0.491
(-1 1 1)	[0 -1 1]	-0.173
(-1 -1 1)	[0 -1 -1]	-0.491
(-1 -1 1)	[-1 0 -1]	0.173
(-1 -1 1)	[1 -1 0]	-0.317

Tensile Behavior

From the quasi-static tensile test and the strains found from the DIC post-processing, the modulus of elasticity was found to be 190 GPa and the tensile yield strength was found to be 149.3 MPa. As shown in Figure 16 the sample showed severe out of plane deformations causing the images to be out of focus and therefore unable to be correlated. This out of plane deformation started at approximately the strain of 1.8% and stress of 151 MPa and severely affected the focus of the images from around the strain of 2.1% and stress of 154 MPa; The test was therefore stopped and the ultimate strength was not found. It is important to note that this was after plasticity had initiated within the polycrystal specimen.

Figure 16. Surface of the sample post-mortem revealing out of plane deformation causing the images to be out of focus for HRDIC purposes.

The tensile yield strength of 149.3 MPa with a low work-hardening rate which is consistent with the findings of the study by Shun et al. on the polycrystal of fcc $Al_{0.3}$CoCrFeNi HEA [91]. They reported a yield drop from the stress-strain curve which have not been observed in our study. They attributed this drop to the nanoprecipitates found through transmission electron microscopy creating Guinier–Preston (GP) zones which are typical of aluminum alloys [102].

Critical Resolved Shear Stress for Slip

SEM micrographs post-mortem are shown in Figure 17 (a). The area of interest is enclosed by a red rectangle in the SEM micrograph on the left. A surface crack is shown using a blue arrow. The micrograph on the right only focuses on the area of interest and the activated slip bands are observed. Figure 17 (b) shows the strain maps in the area of interest at three different global strain levels of 0.004, 0.01. and 0.02. The gray lines are the grain boundaries and the grain where the first slip system activated and is shown with a red dasher box. At the strain of 0.004 no slip activity is observed and at strain of 0.01 the slip activities are first observed. At the strain of 0.02 multiple slip systems at different grains are observed. The region pointed at by the white arrow had severe out of plane deformation. Figure 17 (c) on the left is the post-mortem EBSD IPF Z map. Using the postmortem EBSD data the Schmid factors of the grain are found for all of the possible slip systems. The map of the maximum Schmid factor for each grain with the corresponding slip systems are shown in right. For the grain at which the dislocation slip is first observed, slip tracing is performed using the angle of the activated system with respect to the direction of the load and the orientation of the grain itself using the EBSD data, and the activated slip system and the corresponding Schmid factor is found.

The stress at which dislocations slip are being observed in the grain of interest was found to be 150 MPa. All the slip planes in the three-dimensional space were found using Euler angles

from the EBSD data and the theoretical direction of the plane with the maximum Schmid factor is found on the sample surface. This theoretical plane direction is then compared with the activated slip plane from the DIC strain map. The activated slip system in the grain of interest matched with the slip system with highest Schmid factor. The slip system with the highest Schmid factor of 0.42 was found to be the (-1 1 1)[-1 -1 0] slip system and the CRSS for slip was then calculated to be 63±2 MPa considering several consecutive images at where the dislocation slips are visible from the DIC strain maps.

In polycrystals grain boundaries can limit the dislocation slip and causing dislocation pileups [103]. Also, in finding the CRSS of polycrystals having different grains in different orientations, the Taylor factor can be used. Taylor factor is used for accounting for the averaging of all the different grain orientations within the polycrystal [104] and is approximately 3.1 for an fcc structure [105].

The CRSS for slip in $Al_{0.3}$CoCrFeNi HEA polycrystal at room temperature under tension was found to be 63 MPa. [110]-oriented fcc single micro-crystals of $Al_{0.1}$CoCrFeNi and $Al_{0.3}$CoCrFeNi tested by in-situ micro-compression at the temperature range of 293 to 573 K had slip CRSS to be 239, 260, and 270 MPa for $Al_{0.1}$CoCrFeNi and 244, 267, and 307 MPa for $Al_{0.3}$CoCrFeNi at 573 K, 423 K, and 293 K respectively [106]. The slip CRSS depends on the size pillar size and an inverse power law scaling can be used to extrapolate the bulk CRSS [100]. This difference in the CRSS is due to the use of micropillars in the mentioned studies being manufactured in such a way that they have less defects compared to the polycrystal studied in this research. Further difference when comparing the CRSS from micro-compression tests and polycrystalline tensile tests can be due to the strong work hardening of the micropillars due to their microstructural orientation [106]. Finding the CRSS in polycrystals is essential as in a wide range

of applications polycrystals of the HEAs and metal alloys in general are used. As the different orientations of the grains, grain boundaries and their misorientation angles, and other defects in the polycrystal affect the overall performance, finding the CRSS in polycrystals will provide a more accurate information for practical purposes.

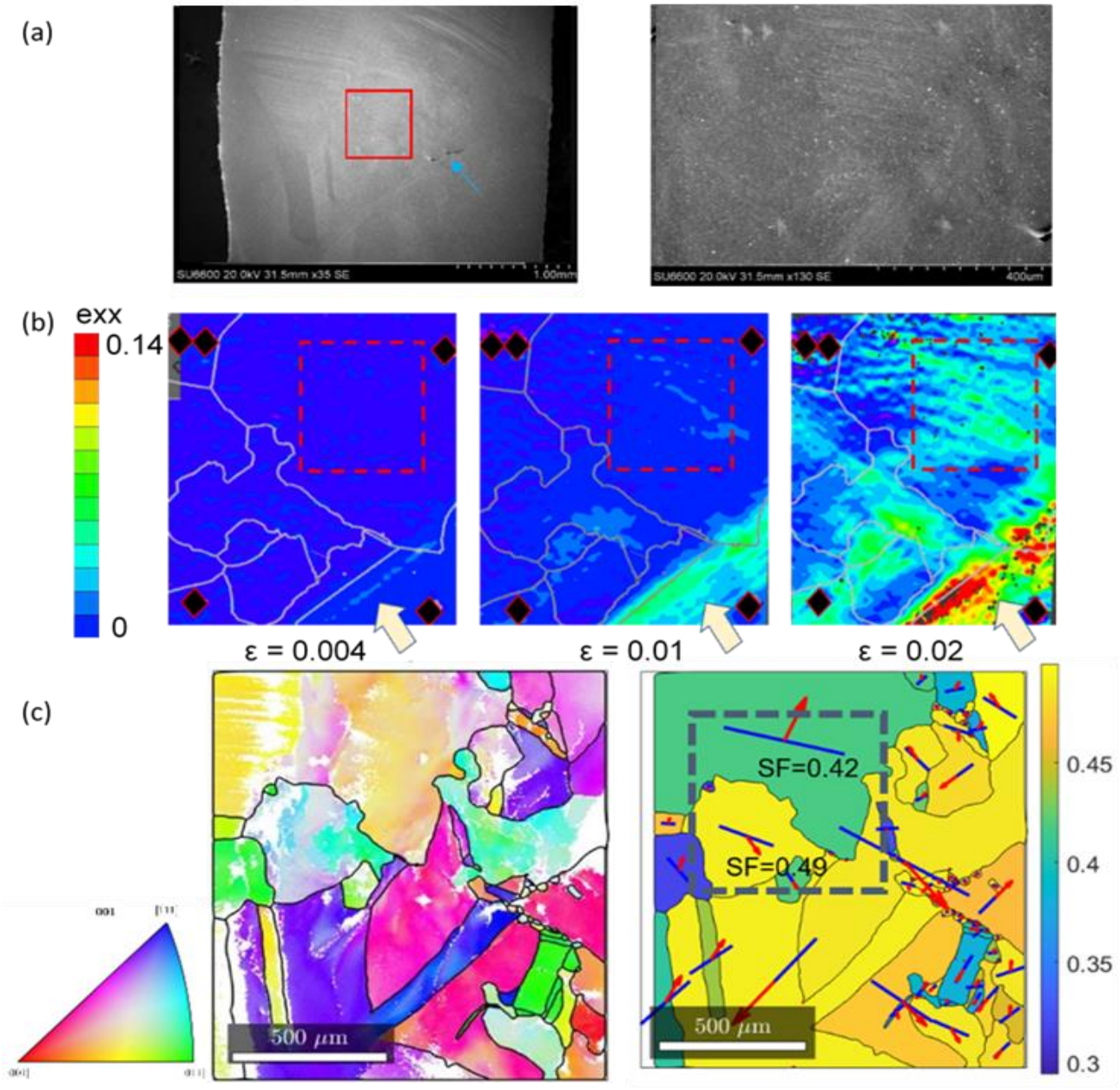

Figure 17. (a) SEM micrographs of the sample post-mortem. (b) Strain map from HRDIC at different strains overlaid with grain boundary map from EBSD. (c) Post-mortem EBSD (left) maximum Schmid factor map (right).

3.4 Conclusions

Tensile tests along with high resolution digital image correlation were run on specimens of $Al_{0.3}$CoCrFeNi single phase fcc HEA. The tensile yield strength was found to be 149.3 MPa and the modulus of elasticity was found to be 190 GPa. The tensile room temperature slip CRSS was found to be 63±2 MPa based on the activated slip system of (-1 1 1)[-1 -1 0] which also had the highest Schmid factor of 0.42.

CHAPTER FOUR: INTRODUCTION TO THE COMPUTATIONAL TECHNIQUES

Parts of this section has been used as part of a journal paper.

Computational approach was used to address the next objectives of this research in which the effect of GB type, GB elemental segregation, and temperature on the deformation twin nucleation and growth is studied in CoCrFeNi HEA bicrystals. This research is done using molecular dynamics simulations and Monte Carlo molecular dynamics simulations. The introduction of the computational techniques is described in this chapter and the specific studied are described in chapters five and six.

4.1 Molecular Dynamics Simulation

In order to study the mechanical behavior of different materials and structures under different loading conditions and to find the underlying physical phenomena, computational methods can be used. Computational methods along with experimental methods can provide a range of information which might not be possible with either of the methods separately. For instance, in experiments one of the limitations can be the characterization tools and scopes resolution or the limited field of view. The limitations for computational methods are the assumptions made and the hardware limitations to run the simulations. Therefore, the choice of computational or experimental study considering the resources is an important choice in approaching a problem.

The computational techniques in computational mechanics and materials science considering the length scale and time scale they are based on are macroscale modeling, for instance finite elements method simulations, microscale modeling, such as crystal plasticity models, atomistic modeling, such as molecular dynamics modeling and ab-initio modeling such as density

functional theory (DFT) calculations. The time scale and length scale of these computational techniques are shown and compared in Figure 18. Depending on the study one or a combination of these methods can be used.

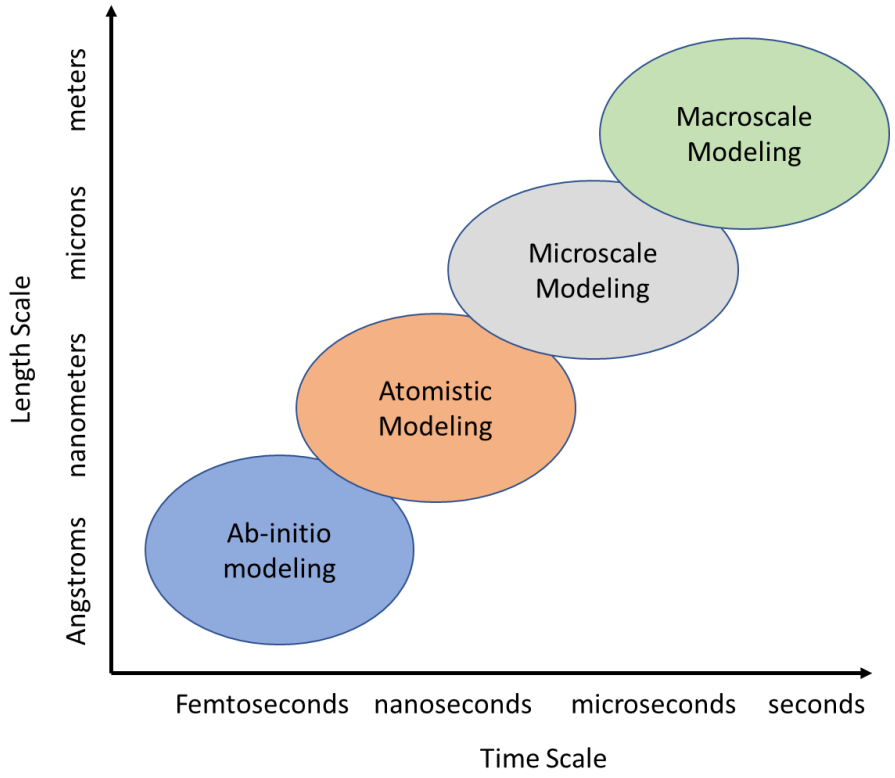

Figure 18. Length scale and time scale of computational simulation methods used in physics, computational materials science, and computational mechanics amongst other fields of research.

In this study the molecular dynamics modeling has been chosen to study the effect of GB types and GB segregation on the mechanical behavior and the deformation mechanisms in CoCrFeNi HEA bicrystals which is thoroughly discussed on the next chapter. Developing bicrystals with specific GBs is not feasible and therefore experimental study is not an option. Amongst the computational techniques, as the deformation mechanisms are known to be in the nanoscale, molecular dynamics simulation is the chosen approach.

Molecular dynamics (MD) simulation method is based on the physical movement of atoms and molecules. In MD simulations, atoms and molecules are considered as basic particles and the Newton's second law of motion, $\boldsymbol{F}=m\boldsymbol{a}$, where $\boldsymbol{F}$ is the force vector, m is the atomic mass, and $\boldsymbol{a}$ is the acceleration vector, is applied on the particles in the simulation [107]. The trajectories of the particles are found at each step of the simulation. A simplified molecular dynamic algorithm can be seen in Figure 19.

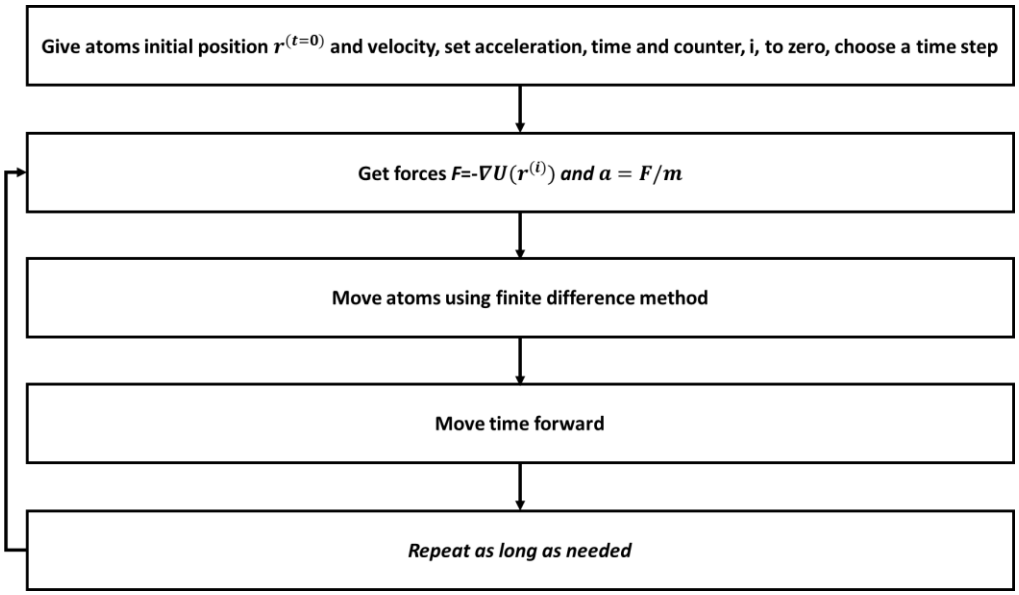

Figure 19. Simplified algorithm of the molecular dynamics simulation.

Initial positions and velocities for each of the atoms are given to the system and by applying the interatomic potential to the entire system through first order derivative of the potential with respect to the atom coordinates, the forces on each atom can be derived. Newton's second law of motion is then used to calculate the accelerations and through the time integration with respect to the time step, the position and velocities of each atom is updated. This procedure can be repeated until the desired material condition is reached [107–109].

At each time step of the simulation, parameters including atom velocities, forces, system dimensions, and energy components can be pulled out. Further through original outputs and

statistical postprocessing properties including the structural and mechanical properties, GB and defect structures, and radial distribution functions can be calculated [107].

From the described procedure based on the algorithm in Figure 19, the importance of the interatomic potential to find the forces on each atom and update the positions and velocities of the atoms in the systems is realized. In the next sections, an overview of the interatomic potentials is presented.

4.2 Monte Carlo Simulation

MD simulations reproduce the small amplitude oscillations of atoms and atoms crossing the barrier from one lattice site to another rarely occurs within the timescale of MD simulations [110,111]. An alternative technique in studying the atom scale processes is using the Monte Carlo methods [111].

Monte Carlo (MC) method is a statistical technique which uses the Boltzmann factor for probability and discrete and random steps for sampling. MC simulations, in contrast to MD simulations is not deterministic. MC method is based on the condition expressed as [111]:

$$W(\boldsymbol{r}'|\boldsymbol{r})P(r) = W(\boldsymbol{r}|\boldsymbol{r}')P(\boldsymbol{r}') \qquad (8)$$

where P(**r**) is the probability of finding a particle at position **r**, and $W(\boldsymbol{r}'|\boldsymbol{r})$is the probability of transition of the particle from one position **r** to another position $\boldsymbol{r}'$. Considering that P follows a Boltzmann distribution we have:

$$\frac{W(\boldsymbol{r}'|\boldsymbol{r})}{W(\boldsymbol{r}|\boldsymbol{r}')} = \exp(-\beta\Delta U) \qquad (9)$$

where $\beta = \frac{1}{k_B T}$, k_B is the Boltzmann constant, T is the temperature in Kelvin, and ΔU is the potential energy change in the system. The method lets the atoms jump around randomly to find the minimum energy state [107]. MC simulation steps thermodynamically probe the favored

configurations. The energy of the current system is computed, random atom is chosen, and a displace/swap is attempted. Then the energy of the new state is computed and the difference between the energy of the two states is found, $\Delta U = U_{swap} - U_{ini}$, where U_{swap} is the energy of the swapped configuration and U_{ini} is the energy of the initial configuration. The move is accepted with the probability $P_{acc} = \min\{1, \exp[-\Delta U/k_B T]\}$ [107,111,112].

Combination of MD/MC simulations can be used to provide a dynamics picture of the system which requires timescales beyond the reach of MD simulations. Combined MD/MC simulations in which some atoms are moved by MD simulations and some are moved by MC simulations, hybrid MD/MC simulations in which atomic displacement description is in part stochastic and in part deterministic, and sequential MD/MC simulations in which MD simulations and MC simulations cycles alternate are among the algorithms in which MD simulations and MC simulations are used together [110,111].

4.3 Interatomic Potentials

In atomistic simulations interatomic potential is of great importance. The interatomic potential defines the interactions of the atoms in the system and the choice of them influences the results of the simulations [113]. Potentials are mathematical expressions of the dependance of the system's energy on its particles' coordinates. Interatomic potential functions for specific systems are proposed and parameterized by using calculated data from first-principles methods and experimental data [107].

Embedded atom method (EAM) potentials are the most common models of atomic bonding used in metallic systems. EAM potentials are conductive to large-scale computer modeling due to their mathematical simplicity and they are rooted in DFT [113]. EAM potentials capture some

electronic effects and meanwhile maintain the potential simplicity by considering the effective electron density at a given atomic site. The mathematical form of the EAM potential is as follows:

$$U_{EAM} = \frac{1}{2}\sum_{i \neq j} U_{ij}(r_{ij}) + \sum_i F_i(\rho_i) \qquad (10)$$

where U_{EAM} is the EAM potential, $U_{ij}(r_{ij})$ is the pair interaction, r_{ij} is the scalar distance between the atoms *i* and *j*, and $F_i(\rho_i)$ is the embedding energy function as a function of electron density ρ_i. The electron density at site i is the superposition of valance-electron clouds from all the other atoms:

$$\rho_i = \frac{1}{2}\sum_{j(\neq i)} \rho_j(r_{ij}) \qquad (11)$$

The electron densities at each MD run are computed at various sites, embedded energies are evaluated and added to the pair potentials. EAM potentials are suitable for most metals, transition metals and especially for fcc metals [107].

4.4 Type of Ensembles

In atomistic simulations each atom moves and behaves differently within the simulation box, but after a proper simulation and equilibrium, the collection of all configurational possibilities with the same macroscopic/thermodynamic properties is considered an ensemble. In MD and MC various ensembles with different controlled variables can be used. The integration of Newton's equations of motion allows the constant-energy surface of a system, however during the molecular simulation other variables might need to be held constant [107,114].

The variables that are attempted to be held constant are number of atom N, volume V, pressure P, temperature T, energy E, and enthalpy H. In all of the ensembles the number of particles, N, is conserved and the available ensembles are NVE having constant volume and energy, NVT having constant volume and temperature, NPT having constant pressure and temperature, and NPH having constant pressure and enthalpy [107].

NVE ensemble is obtain by solving the Newton's equation without pressure and temperature controls. This ensemble is known as the microcanonical ensemble and the energy is conserved when this ensemble is generated. In this method desired temperature cannot be achieved due to not using temperature control methods when facilitating the energy flow and it is not suitable for equilibrium [107,114]. In NVT ensemble the temperature is controlled using direct temperature scaling during initialization and temperature bath coupling during the data collection. This ensemble is called the canonical ensemble and the volume is kept constant during the simulation runs [107,114,115]. In the NPT ensemble temperature and pressure are both controlled, and the pressure is adjusted by volume change. This ensemble can be used during equilibrium and when the correct pressure, volume, and densities are of importance during the simulation [107,116]. It is noteworthy that in these ensembles the goal is not to have a constant temperature but rather to have the desired temperature as the average temperature of the systems.

4.5 Conclusions

In this chapter the fundamentals of the computational methods used in this research has been covered. In the following chapters, the atomistic modeling study of the effect of GB type, GB elemental segregation, and temperature on the deformation twin nucleation in CoCrFeNi HEA bicrystals are explained. Specific material and methods of the research are discussed in the next chapters.

CHAPTER FIVE: EFFECT OF GRAIN BOUNDARY TYPE ON THE MECHANICAL BEHAVIOR IN COCRFENI HIGH ENTROPY ALLOYS

Parts of this section has been used as part of a journal paper.

5.1 Background and Motivation

CoCrFeNi is in the 3d transition metal HEA group and it is in the family of CoCrFeMnNi HEA also known as the Cantor alloy. CoCrFeNi is an equimolar HEA having 25% of each element. CoCrFeNi HEA similar to most if the HEAs in the Cantor family shows simultaneous strength and ductility for a range of temperature. Strength and ductility both increase as the temperature decrease to cryogenic temperature [12,54]. This has been attributed to the nucleation and growth of deformation nano-twins as an additional mode of plastic deformation [12,54]. This is typical of fcc metals and alloys with low stacking fault energy. CoCrFeNi is a single phase fcc HEA with a stacking fault energy of 30-33 mJm^{-2} [19,117,118] which is considered within the range energetically necessary for deformation twins to nucleate. Also, as mentioned before, HEAs have local compositional and chemical variations which results in local variation of stacking fault energy in the lattice, making parts of the lattice more favorable for twin nucleation that others.

It has been observed experimentally that deformation twins nucleate from defects in the alloy for instance the GB. Recently, nucleation of deformation twin from GB has been observed in CoCrFeMnNi HEA, shown in Figure 20 [13]. This observation has also been made in studies on other metals. Therefore, GB as preferential cite for twin nucleation needs to be further studied.

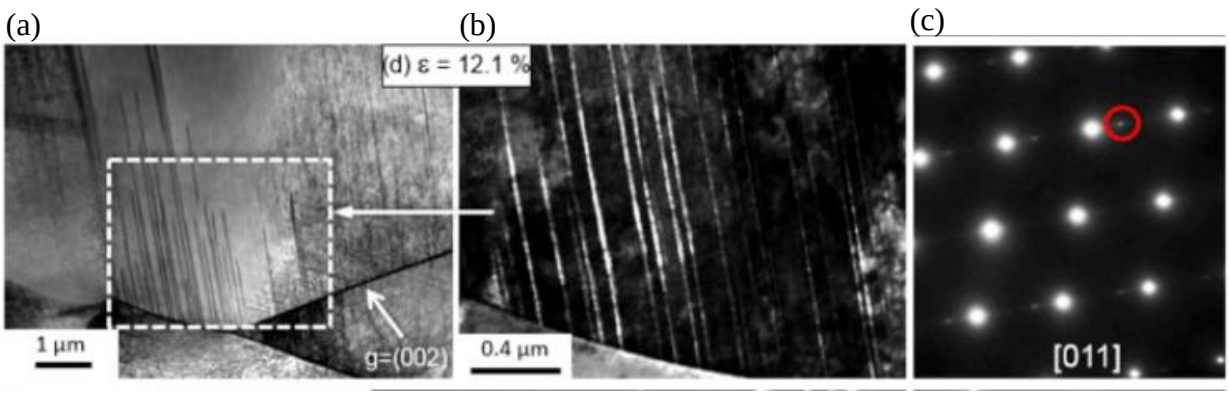

Figure 20. TEM (a) bright field, (b) dark field, (c) diffraction pattern showing twin nucleation from grain boundaries in CoCrFeMnNi HEA [13].

GB characteristics can have an effect on the continuum level material properties such as ductility and strength [119]. GB properties such as disorientation angle, ∑ value, and boundary energy vary with boundary types [119]. In GB engineering, considering the overall material properties, the goal is to enhance or reduce boundary types. Five degrees of freedom in the crystallographic space can be used to define GB types, three for the relative angles between two neighboring grain and two for the relative orientation of the boundary plane to the grains [119].

Considering the experimental results that grain boundaries are preferential sites for twin nucleation, and knowing that different GB types can effect material properties in general, it is important to understand the effect of different GB types on the twin nucleation and growth in fcc HEAs. To do so, bicrystals of the HEAs having different GB types need to be tested under tension. However, growing bicrystals with specific GBs is not feasible and computational techniques need to be used. In this study, MD has been used to model and mechanically test bicrystals of CoCrFeNi HEA to answer the following question:

- Does GB type influence the twin nucleation in fcc HEAs?

- What is the critical resolved shear stress for twin nucleation in CoCrFeNi? Does GB type and temperature influence it?
- What is the effect of adding Mn in the twinning behavior of fcc HEAs?

The results of this research further help with understanding the physical phenomena and the alloy development to reach to even better properties in metal alloys by GB engineering.

5.2 Materials and Methods

As an overview of the methods, large-scale atomic/molecular massively parallel simulator (LAMMPS) which is a classical molecular dynamics code was used in this study [120]. Clemson University Palmetto Cluster was used to run the simulations. Atomic positions and visualizations were done using open visualization tool (OVITO) [121]. OVITO and MATLAB were used for post processing of the data.

Symmetric Twist Grain Boundaries

A series of CoCrFeNi bicrystlas with <110> symmetric twist grain boundaries (STGBs) were generated using the second nearest-neighbor modified EAM interatomic potential from the work by Choi et al. [69] on CoCrFeMnNi HEA. Experimental mechanical properties and solid solution hardening effects observed experimentally has have been successfully reproduced using this potential [69]. The bicrystals of the CoCrFeNi HEA with prescribed GB geometries were constructed by creating a fully periodic atomistic system from two half crystals. Each of the half crystals was rotated to result in the specified misorientation angle of the planar GB between the halves. A series of rigid body translation was performed on the bicrystals within the GB plane resulting in equilibrated GB structure (γ-surface method) [122,123]. A schematic of the bicrystal model is shown in Figure 21. The different GB sigma values, corresponding misorientation angles

and the crystals x-axis for the upper and lower grains are shown in Table 5. The sigma values are shown in an increasing order where 1/sigma corresponds to the coincidence lattice points.

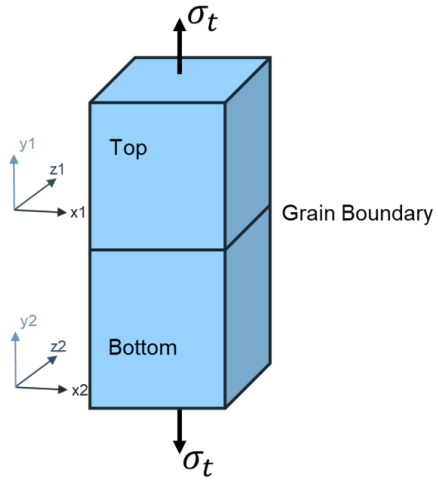

Figure 21. Schematic of the bi-crystal structure. The top and the bottom crystals are shown with their local corresponding coordinate systems.

The target dimensions of the bicrystal geometry were set to 100 Å × 600 Å × 100 Å with small variations for each of the bi-crystals with different grain boundaries and the number of atoms for each of the simulation boxes was 700000 with variations for each of the bi-crystals with different grain boundaries.

Table 5. Sigma values, corresponding misorientation angles, and the upper and lower crystals x-axis for all the grain boundaries.

Sigma	**Misorientation Angle**	**[hkl] x-upper/ [hlk] x-lower**
3	70.53	$[1\bar{1}\bar{1}]/[\bar{1}1\bar{1}]$
9	38.95	$[2\bar{2}\bar{1}]/[\bar{2}2\bar{1}]$
17	86.60	$[2\bar{2}\bar{3}]/[\bar{2}2\bar{3}]$
19	26.53	$[3\bar{3}\bar{1}]/[\bar{3}3\bar{1}]$
27	31.6	$[1\bar{1}\bar{5}]/[\bar{1}1\bar{5}]$
33	58.98	$[2\bar{2}\bar{5}]/[\bar{2}2\bar{5}]$
41	55.88	$[4\bar{4}\bar{3}]/[\bar{4}4\bar{3}]$
43	80.63	$[3\bar{3}\bar{5}]/[\bar{3}3\bar{5}]$
51	23.07	$[5\bar{5}\bar{1}]/[\bar{5}5\bar{1}]$

Mechanical Testing

Prior to the mechanical testing the system was relaxed at the desired temperatures using the NPT ensemble. Nose-Hoover style isothermal-isobaric (npt) fix command was used [124–128]. The barostatting can be done either as iso (hydrostatic) and aniso to specify all 6 components of an external stress tensor. Iso means coupling all 3 diagonal components together (hydrostatic pressure) and dilate/contract all the dimensions together. The 77 K thermal equilibration simulations were run using the aniso setting to have the *x*, *y*, *z*, dimensioned controlled independently for 300000 steps (300 picoseconds).

The mechanical tests of uniaxial tension were performed with the strain rate of 5×10^{8} s^{-1} at the desired temperatures for each of the grain boundaries and using the NPT ensemble the pressure in the transverse directions was set to be zero. Layers of atoms were fixed on the top part and bottom part. The atoms positions in these parts were fixed relative to each other. The thickness of this fixed part is around 25 Å and was used to impose the forces on the dynamic atoms and as imposed boundary conditions, Figure 22. The bottom part did not move during the simulation and the top part will move with the applied velocity to mimic the experimental tensile test. Periodic boundaries were used along the *x* and *z* dimensions for the simulation box. But along for the *y*-direction the shrink-wrap boundary condition was used for the mechanical testing. The tensile tests were run for 300000 steps (300 picoseconds) at the desired temperature of 77 K. The LAMMPS codes of the simulations are presented in Appendix A.

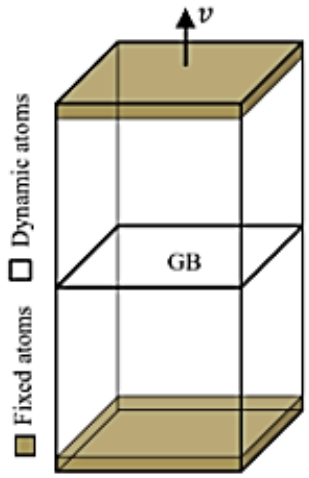

Figure 22. Schematic of the bi-crystal simulation box and the fixed atoms regions.

Post Processing

After the mechanical tests, the output data was used and post-processed to plot the stress-strain curves and find the material properties. Stress was found using the compute stress/atom command in LAMMPS. This command computes per-atom stress tensor for each atom [129]. Strain was calculated from the change in length in the *y* direction over the initial length not considering the fixed parts. Using the dump files and in OVITO the dislocation extraction algorithm (DXA) was used to analyze the dislocations. The centrosymmetric parameter, common neighbor analysis (CNA), and polyhedral template matching (PTM) algorithm were used to find the crystal structures and the orderings.

5.3 Results and Discussion

Elemental Percentage and Distribution

The percentages of each of the four elements in the simulation box was investigated to assure elemental percentages of 25% in each of the bi-crystal models after randomly assigning the four elements Co, Cr, Fe, Ni. The concentrations of each element for each of the bicrystals with specific grain boundaries are shown in Table 6. As shown the concentration deviations from the 25% are negligible.

Table 6. Elemental concentration for each of the bi-crystals models with different GB sigma values

GB sigma value	Fe%	Ni%	Cr%	Co%
17	25.02	25.07	24.99	24.92
19	25.05	25.06	24.93	24.97
27	24.03	24.90	25.04	25.04
33	24.92	24.96	25.15	24.97
41	24.96	25.02	25.04	24.99
43	25.02	24.98	25.02	24.98
51	25.01	24.97	24.98	25.04

Uniform and randomized distribution of the four elements Co, Cr, Fe, and Ni in the bicrystal models was also investigated visualizing the in OVITO shown in Figure 23 and also by calculating short-range order (SRO) parameters for the possible nearest bonds. Radial distribution function (RDF) with cutoff radius of 3.2 Å in OVITO was used. RDF shows the probability of a particle at a distance ‘r’ from another particle and it can be used to check the SRO. The equation for the RDF g(r) is,

$$g(r) = \lim_{dr \to 0} \frac{p(r)}{4\pi\left(N_{pairs}/V\right)r^2 dr} \qquad (12)$$

where r is the distance between a pair of particles, V is the total volume of the system, N_{pairs} is the number of unique pairs of atoms, and $p(r)$ is the average number of atom pairs found at a distance between r and $r + dr$ [130]. As shown in Figure 24 the probability of existence of each of the pair are close to each other insuring randomized distribution of the elements in the HEA bi-crystal model after randomly assigning the four elements in the bicrystal models. The RDF shown is for GB sigma 33 but the results were consistent for other GBs.

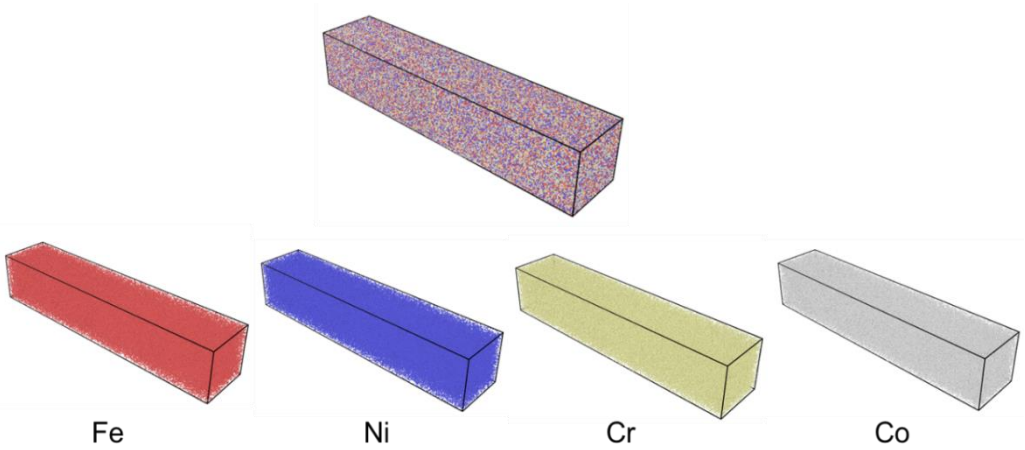

Figure 23. Visual inspection of the uniform distribution of each element in the bi-crystal model for GB sigma 33.

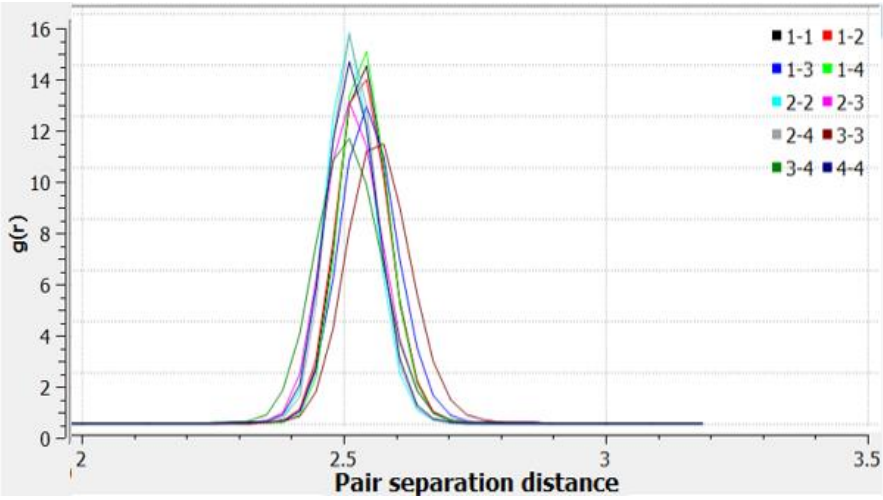

Figure 24. RDF function for GB sigma 33 at 77 K after randomly assigning the elements to the model. Elements 1, 2, 3, 4 are Fe, Ni, Cr, Co,

Mechanical Behavior

The 77 K tensile mechanical behavior of the CoCrFeNi HEA bicrystals is first examined and compared to the results from the same study on the CoCrFeMnNi HEA bicrystals (from our collaborator). The stress strain curves from the mechanical testing at 77 K, for <110> for CoCrFeNi (this study) and CoCrFeMnNi (collaborator) are shown in Figure 25.

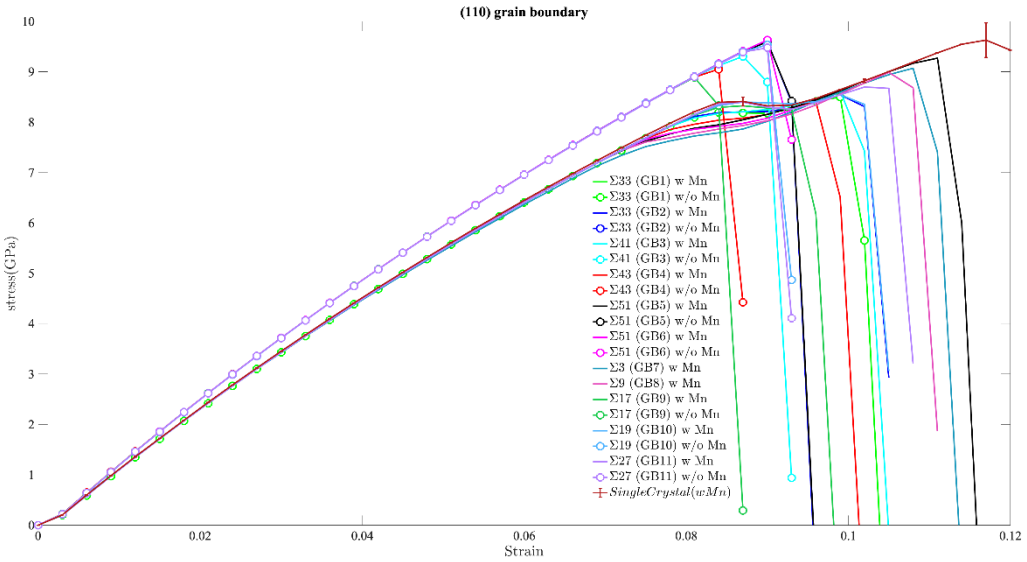

Figure 25. Stress-strain curves for CoCrFeNi and both CoCrFeNi and CoCeFeMnNi bi-crystals with different <110> symmetric grain boundaries

As seen from the stress strain curves, different grain boundaries resulted in different stress-strain curves for each alloy bicrystal. Overall, yield strength of CoCrFeNi HEA were higher than that of CoCrFeMnNi, which matches with what is observed from experiments [20,131]. Generally, the mechanical behavior of the two HEA are similar to austenitic steel [11,20,117].

From the manufacturing and cast-ability point of view, manganese severely partitions into liquid region during the manufacturing having a solidification partitioning factor of less than one [132]. From the corrosion point of view, adding manganese to CoCrFeNi impairs corrosion resistance of the solid solution and deteriorates the pitting corrosion of the alloy as shown in Figure 26 [5]. From the mechanical properties point of view, adding manganese lowers the yield and ultimate strength and therefore it is detrimental to the strength [11,19,20,117,131], also observed from the this research for all of the GBs studied. Both CoCrFeNi and CoCrFeMnNi showed promising properties to be used at cryogenic temperatures but overall CoCrFeNi HEA is a better candidate.

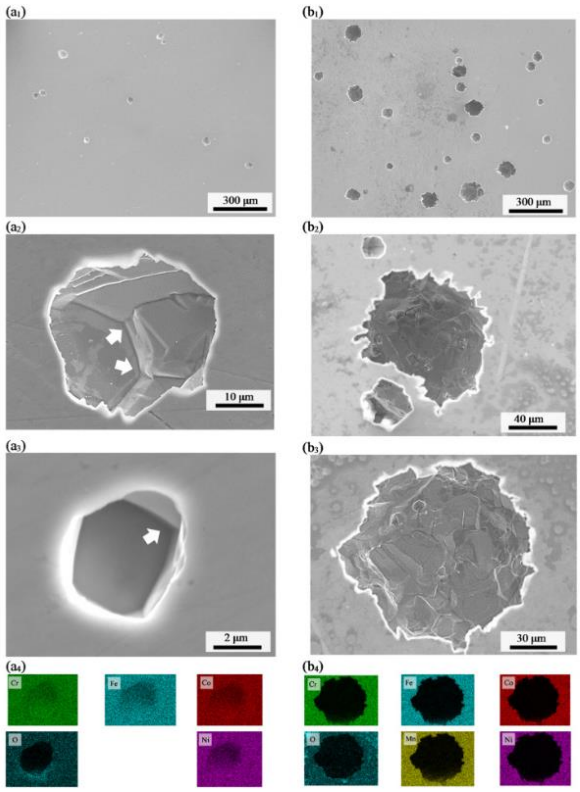

Figure 26. SEM and EDS micrographs of Pits formed at 75 °C at applied potentials of +0.2 V vs. SCE in 0.1 M NaCl on ($a_{1–3}$) CoCrFeNi and ($b_{1–3}$) CoCrFeMnNi [5].

To further investigate the effect of the geometry of GBs on the mechanical behavior of the CoCrFeNi HEA bicrystals, the yield stress as a function of GB misorientation angle (twist angle) are shown in Figure 27. An overall decreasing trend of the yield strengths with the increase in the GB misorientation angle is observed. The GB with the sigma value of 17 corresponding to the highest misorientation angle of 86.6º had the lowest yield strength of 8.89 GPa. The GB with the sigma value of sigma 51 corresponding to the lowest misorientation angle of 23.07 had the highest yield strength of 9.59 GPa. There are two discrepancies observed for GBs with sigma values of 33 and 43 with the corresponding misorientation angles of 58.98º and 55.88º.

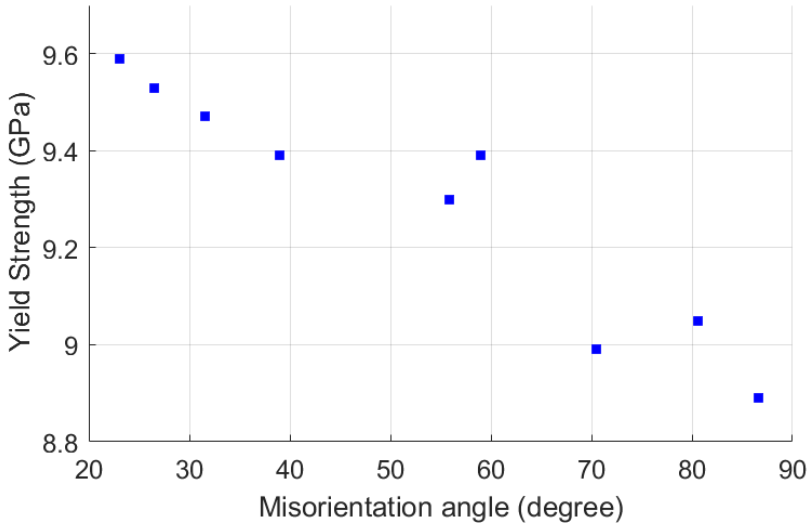

Figure 27. Yield strength versus misorientation angles of the GBs for each of the CoCrFeNi bicrystals tested under tension at 77K

Deformation Mechanism

For all of the CoCrFeNi HEA bicrystals, the partial dislocations nucleated from the GBs and further grew in the bulk crystal. This facilitated the nucleation of deformation twins and confirmed GBs as nucleation sites of deformation twins as also observed experimentally [13]. As a demonstration the GB region of the sigma 33 GB bicrystal is shown as the dislocations and

further deformation twins are nucleating from the GB (Figure 28). The other GBs showed the same deformation nucleation behavior.

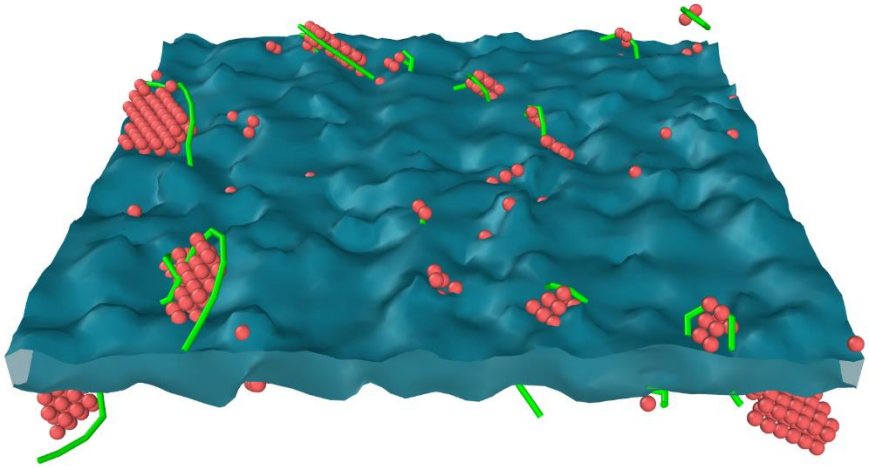

Figure 28. The grain boundary for the CoCrFeNi bicrystal with sigma 33 region is shown with the Shockley partial dislocation shown in green and the HCP phase shown in red. Demonstrating the nucleation of partial dislocations and deformation twins.

5.4 Conclusions

Using MD simulations, the tensile behavior of CoCrFeNi HEA bicyrstals with different symmetric twist grain boundaries were studied at 77 K and compared with the results from CoCrFeMnNi HEA bicrystals. Addition of Mn to CoCrFeNi HEA is detrimental to the yield and ultimate strength observed from experimental and MD modeling studied. Also adding Mn is detrimental for manufacturing, corrosion, and strength of the material. Therefore, overall, the performance of the CoCrFeNi HEA a better than CoCrFeMnNi HEA. Twin nucleation started from the GBs, confirming GBs as preferential sites for twin nucleation. GB types affect the deformation twin behavior of the HEA bicrystals. Overall, with the increase of the misorientation angles the yield strength and the strength for twin nucleation decrease. The results of this research confirmed the effect of the GB types on twin nucleation in low stacking fault energy fcc HEAs and can further be used in GB engineering to populate the alloy with the preferential GBs.

CHAPTER SIX: EFFECT OF TEMPERATURE AND GRAIN BOUNDARY ELEMENTAL SEGREGATION ON THE MECHANICAL BEHAVIOR AND DEFORMATION MECHANISMS IN COCRFENI HIGH ENTROPY ALLOYS

Parts of this section has been used as part of a journal paper.

6.1 Background and Motivation

In general defects in the lattice are thermodynamically preferable sites for solution trap, and therefore elemental segregation when sufficient solute diffusion occurs. Grain boundaries in metal alloys are defects that affect material properties such as tensile strength, strain hardening, fatigue resistance, and fracture toughness [133,134].

Grain boundaries are planar defects and require 5 parameters to be characterized and they cannot be considered as scalar objects having homogeneity. Therefore, specifically in HEAs, grain boundaries are considered as potential sites for elemental segregation. Experimentally, to explore the chemical homogeneity and possible elemental segregation down to the atomic level, local electrode probe tomography (APT) can be used (Figure 29) [59,135,136].

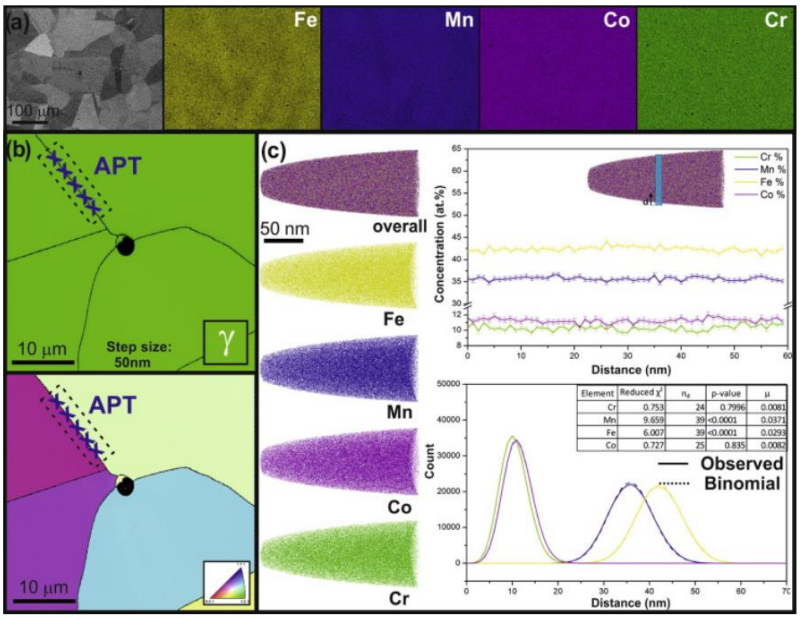

Figure 29. Characterization of non-equiatomic $Fe_{40}Mn_{40}Co_{10}Cr_{10}$ HEA using (a) SEM and EDS, (b) EBSD, and (c) APT [59].

Computationally Frolov et al. [137] and Zhu et al. [138] developed performed a grand-canonical GB structure search and identify a GB phases with different structures in pure metals. Also, Wynblatt and Chatain [139] in a recent computational study have shown using MCMD simulations that both Cr and Mn segregate to GBs in the CoCrFeMnNi HEA. Nano-scale elemental segregation as a potential factor affecting twin nucleation at grain boundaries is an important consideration that has not been studied in HEAs.

In the previous chapter the effect of GB type was investigated. In this study, the bicrystals with different <110> symmetric twist GBs introduced in the previous chapter were chemically equilibrated using Monte Carlo molecular dynamics (MCMD) simulations. Then the bicrystals were tested under tension at three different temperatures of 77K, 300K, and 600K using molecular dynamics simulations to answer the following research questions:

- Does any of the Co, Cr, Fe, and Ni segregate at the GB in CoCrFeNi HEAs?
- Does elemental segregation at GBs influence the twin nucleation for different GB types?

The results of this research further can be used for designing and developing HEAs with improved properties through GB engineering and segregation engineering.

6.2 Materials and Methods

The bicrystals with the different symmetric twist GBs introduced and developed in the research presented in Chapter 5 are going to be used in this research. The sigma values, misorientation angle and the upper and lower crystal *x*-axis is given in Table 7.

Monte Carlo Molecular Dynamics

To study the elemental segregation at the GB and its effect on the twinning behavior of the alloy before running the tensile tests the system was chemically equilibrated using Monte Carlo

molecular dynamics (MCMD). MCMD is possible in LAMMPS using the atom/swap Fix Style command. This fix performs MC swaps of pairs of atoms. "*fix nvt*" was used to move all the atoms in the simulation domain with the regular time integration displacement which results in MCMD simulation. In the case of fix nvt the Nose-Hoover style equation of motion generate positions and velocities are sampled from canonical ensembles [124–128]. The potential energy, and the total energy were evaluated prior and after the MCMD runs. A MATLAB code was written to plot the change in elemental distribution along the *y*-axis of the simulation box prior and after the MCMD runs by cutting several bins parallel to the GB.

Table 7. Sigma values, corresponding misorientation angles, and the upper and lower crystals *x*-axis for all the grain boundaries.

Sigma	**Misorientation Angle**	**[hkl] *x*-upper/ [hlk] *x*-lower**
17	86.60	$[2\bar{2}\bar{3}]/[\bar{2}2\bar{3}]$
19	26.53	$[3\bar{3}\bar{1}]/[\bar{3}3\bar{1}]$
27	31.6	$[1\bar{1}\bar{5}]/[\bar{1}1\bar{5}]$
33	58.98	$[2\bar{2}\bar{5}]/[\bar{2}2\bar{5}]$
41	55.88	$[4\bar{4}\bar{3}]/[\bar{4}4\bar{3}]$
43	80.63	$[3\bar{3}\bar{5}]/[\bar{3}3\bar{5}]$
51	23.07	$[5\bar{5}\bar{1}]/[\bar{5}5\bar{1}]$

Mechanical Testing

Prior to the mechanical testing the system was relaxed at the desired temperatures using the NPT ensemble. Nose-Hoover style isothermal-isobaric (npt) fix command was used [124–128]. The 77K, 300K, and 600K thermal equilibration simulations were run using the aniso setting to have the *x*, *y*, *z*, dimensioned controlled independently for 300000 steps (300 picoseconds).

The mechanical tests of uniaxial tension were performed with the strain rate of 5×10^{8} s^{-1} at the desired temperatures for each of the grain boundaries and using the NPT ensemble the pressure in the transverse directions was set to be zero. Layers of atoms were fixed on the top part

and bottom part. The atoms positions in these parts were fixed relative to each other. The thickness of this fixed part is around 25 Å and was used to impose the forces on the dynamic atoms and as imposed boundary conditions, Figure 22. The bottom part did not move during the simulation and the top part will move with the applied velocity to mimic the experimental tensile test. Periodic boundaries were used along the *x* and *z* dimensions for the simulation box. But along for the *y*-direction the shrink-wrap boundary condition was used for the mechanical testing. The tensile tests were run for 1000000 steps (1000 picoseconds).

Post Processing

After the mechanical tests, the output data was used and post-processed to plot the stress-strain curves and find the material properties. Stress was found using the pressure in the y direction output from LAMMPS rescaled based on the dynamic portion. The pressure computation in LAMMPS is on the entire systems of atoms using the equation below [129]:

$$P = \frac{Nk_BT}{V} + \frac{\sum_i^{N'} r_i \cdot f_i}{dV} \qquad (13)$$

where N is the number of atoms in the system, k_B is the Boltzmann constant, T is the temperature, d is the system dimension, V is the volume of the system, and r_i and f_i are the position and force vector of atom i. As the top and bottom of the bi-crystals are fixed the pressure calculated by LAMMPS needs to be rescaled. Strain was calculated from the change in length in the y direction over the initial length not considering the fixed parts. Using the dump files and in OVITO the dislocation extraction algorithm (DXA) was used to analyze the dislocations. The centrosymmetric parameter, common neighbor analysis (CNA), and polyhedral template matching (PTM) algorithm were used to find the crystal structures and the orderings.

6.3 Results and Discussion

Chemical Equilibrium Results

After the MCMD runs, the temperature, total energy, and potential energy have been plotted versus the steps of MCMD simulations and are shown in Figure 30 for GB with sigma 33 at temperature of 77 K, 300 K, and 600 K. The results for other grain boundaries were similar. Due to the high entropy of configuration in these alloys, reaching to the chemical equilibrium and lowest energy state is not expected. As observed in Figure 31 the volume of the system changes with the MCMD simulations. Increase in the volume is observed with the decrease in potential energy.

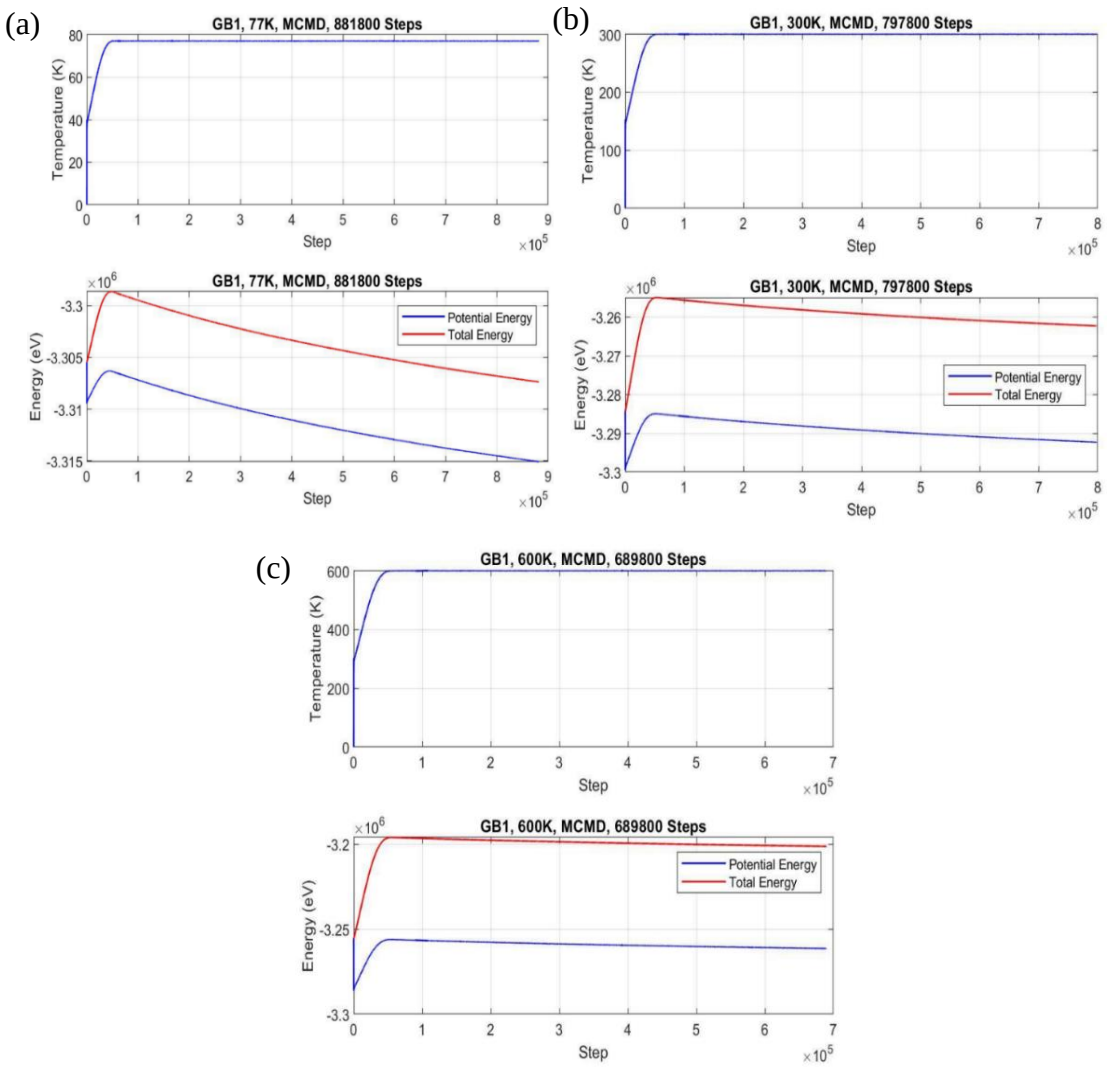

Figure 30. Temperature, total and potential energy versus the steps during the MCMD simulations for GB with sigma of 33 at (a) 77 K, (b) 300 K, and (c) 600 K.

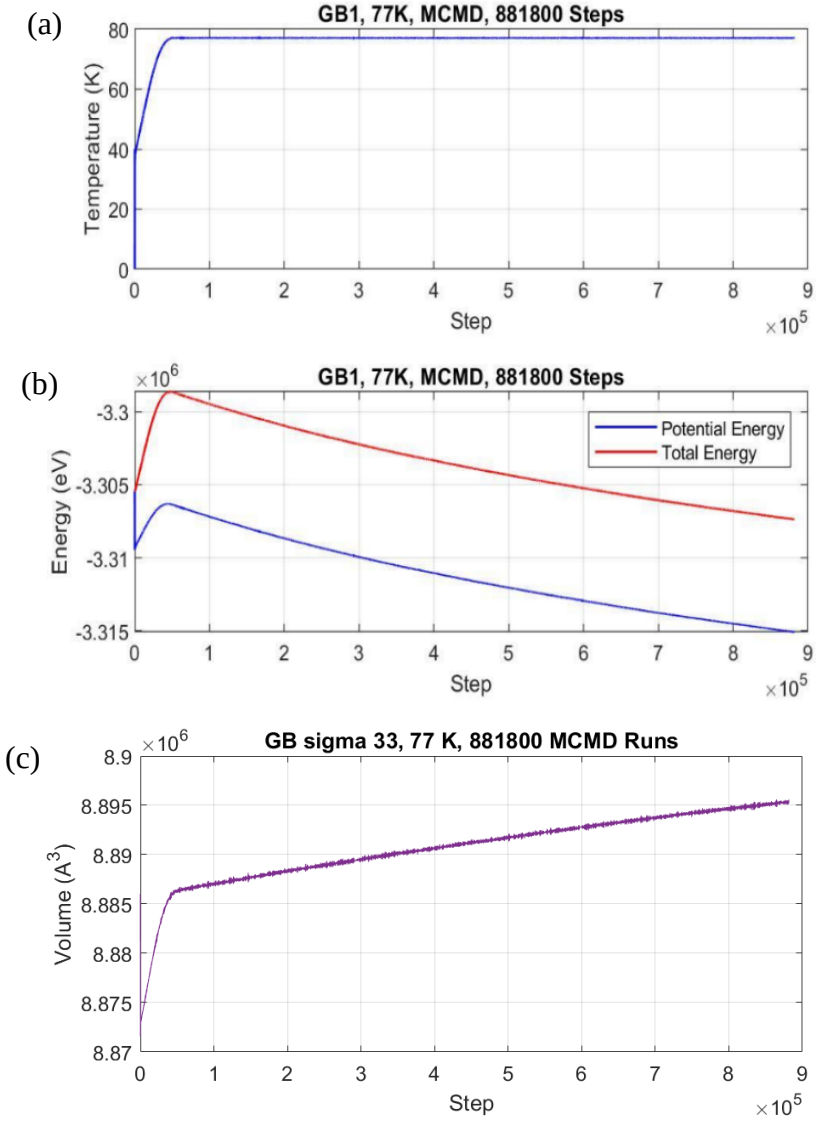

Figure 31. GB1 with sigma 33, at 77 K results from 881800 MCMD runs, including (a) the temperature, (b) the potential, and total energy, and (c) the volume of the system.

The distribution of the elements along the loading direction (y-direction) was plotted for the two cases as well as for before running any MCMDs using the snapshot dump files providing each elements configuration within the simulation box. A MATLAB code was written to extract the information from the snapshot dump file and plot the elemental distribution along the *y*-axis. In the dump files the atom coordinates are written in the scaled format from 0 to 1 and therefore

this scaled number should be multiplied by the length of the box in each direction and then be added to the lower dimension of the box in that direction.

The number of bins was chosen to be 32 such that, the elemental percentage change can be captured for the GB region. This was based on this consideration that the boundary thickness is roughly ten layers of atom (20 Å) [140]. The number of bins was programmed to be modifiable in case of additional/unforeseen considerations. The *y*-axis length of the box and the number of atoms for GB1 (sigma 33) at 77 K before, at the 882000, and at 891000 steps of MCMD were 619.08 Å and 774048 respectively. The graphs of the elemental percentages are shown in Figure 32 for the three snap shots. The bin related to the GB is enclosed by red dashed lines. It can be observed from the graphs that before running the MCMD simulations, at the GB bin, the elemental percentages of Fe, Ni, and Co, were in the same range but for Cr this percentage is higher, After MCMD runs the GB became more Cr-rich and Ni-deficient. This trend continues as more MCMD simulations are run. It is also noteworthy that although this trend on increase in Cr and decrease Ni was observed, this change did not significantly affect the number of atoms in the GB bin. In the boundary bin the number of atoms was roughly 24186 therefore the Cr element percentage in the GB bin changed from 25.9% to 26.1% to 27.4%.

Mechanical Behavior

The mechanical tests were run for all the GBs at the three different temperatures of 77K, 300K, and 600K, using the restart files from MCMD runs. The stress-strain curves are shown for each GB at the three different temperatures in Figure 33. The mechanical properties for all the grain boundaries at different temperatures, modulus of elasticity and yield strength are shown in Table 8. In order to find the modulus of elasticity, due to the elastic region being non-linear, region

of the curve before the yield point was selected, a second order degree polynomial was fit to the data for different ranges of data from the beginning to the yield point and then averaged.

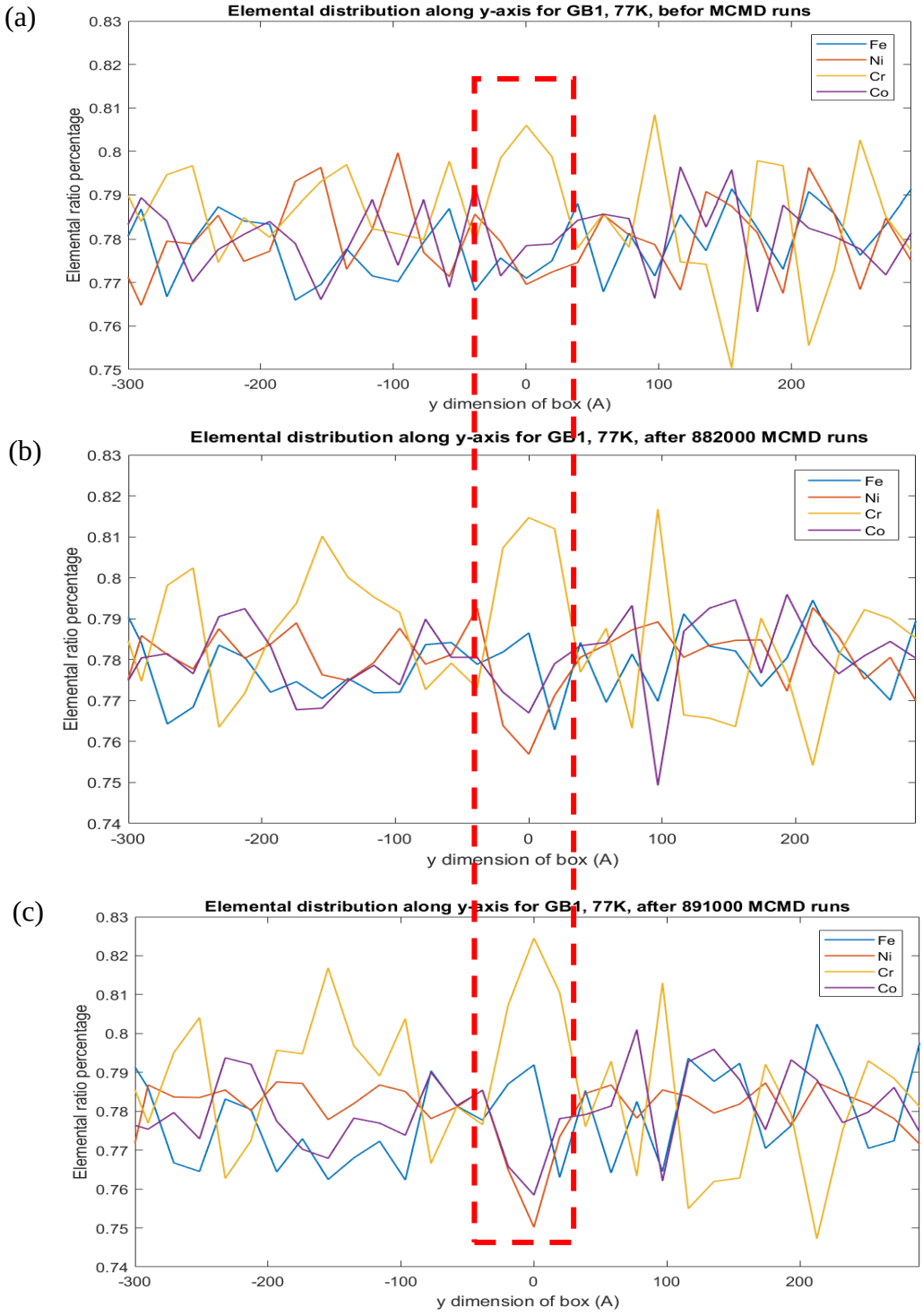

Figure 32. Elemental distribution along the y-axis length of the simulation box, for GB1, at 77 K, (a) before MCMD runs, (b) after 882000 and (c) after 891000 MCMD runs. Grain boundary region is enclosed by the red dashed line.

(a)

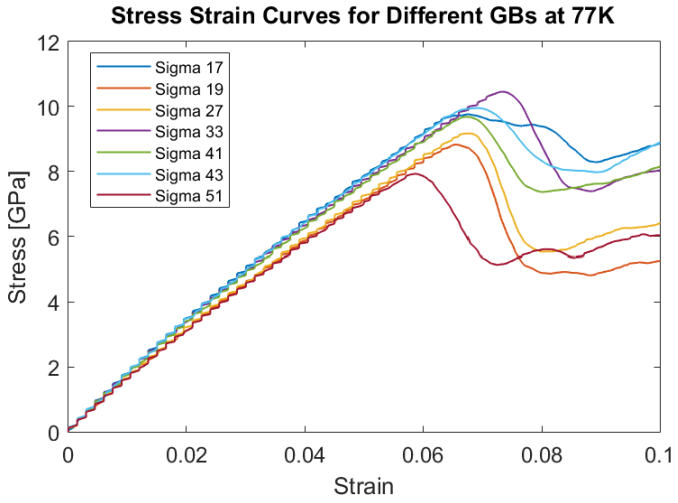

(b)

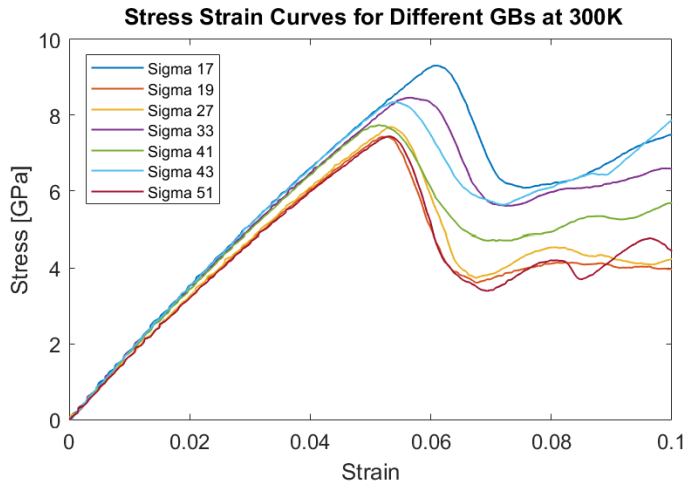

(c)

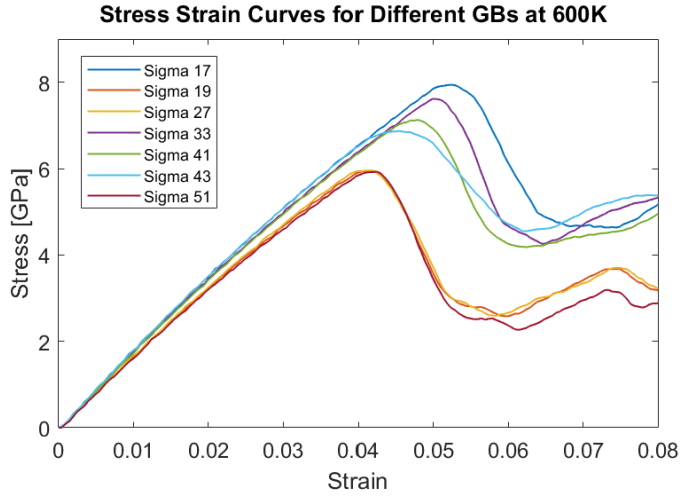

Figure 33. Stress-strain curves for the seven GBs and at three temperature (a) 77 K, (b) 300 K, and (c) 600 K.

Table 8. Mechanical properties for all the GBs and at all the temperatures for the uniaxial tensile test.

Sigma	Misorientation Angle	Temperature [K]	Modulus of Elasticity [GPa]	Yield Strength [GPa]	Yield Strain %
27	31.6	77K	170.2±0.5	9.17	6.8
		77K, 2nd trial	170.4±1.0	9.08	6.6
		300K	173.9±0.8	7.69	5.3
		600K	179.3±0.6	5.96	4.2
		1050K	169.3±0.7	4.88	3.6
19	26.53	77K	166.7±0.5	8.3	6.6
		300K	176.5±0.5	7.43	5.3
		600K	177.8±0.7	5.95	4.1
		1050K	165.8±1.2	4.92	3.8
17	86.60	77K	187.6±0.8	9.76	6.8
		300K	190.2±0.6	9.31	6.1
		600K	191.1±0.2	7.94	5.2
51	23.07	77K	165.7±0.4	7.92	5.9
		300K	174.4±0.3	7.44	5.3
		600K	176.2±0.8	5.93	4.2
43	80.63	77K	180.9±1.1	10.10	6.9
		300K	189.3±0.3	8.35	5.4
		600K	190.5±0.3	6.87	4.5
41	55.88	77K	177.6±0.9	9.67	6.7
		300K	186.9±0.5	7.74	5.1
		600K	186.4±0.6	7.12	4.8
33	58.98	77K	181.1±1.1	10.45	7.3
		300K	186.6±0.5	8.46	5.6
		600K	188.1±0.2	7.62	5.0

The stress strain behavior and material properties were different for different GBs and for the different temperatures for each of the GBs. Yield strength and yield stress increased with the decrease in temperature for all the GBs. The modulus of elasticity increased with the increase of temperature. Considerable softening generally occurs at temperatures above about 0.6 of the absolute melting point of an alloy. The melting point of CoCrFeNi is 1700 K [141] and therefore tensile tests were done at 1050 K for two of the GBs (sigma 27 and sigma 19) to capture the trend for the modulus of elasticity with the increase of temperature. As expected, the modulus was lower than that of all the other three temperatures for both GBs tested.

To further investigate the effect of the geometry of GBs on the mechanical behavior of the CoCrFeNi HEA bicrystals, the mechanical properties as a function of the GB misorientation angle (twist angle) at the three different temperatures are shown in Figure 34. The modulus of elasticity for all the temperatures increased with the increase in misorientation angle except for sigma 27 and sigma 33 with the corresponding misorientation angles of 31.6º and 58.98º. Yield strength and yield stress also show an overall increase with the increase of the misorientation angles with discrepancies specifically for the 77 K results.

Deformation Mechanism

To investigate and characterize the activated deformation mechanisms, the dump files generated during the mechanical testing were looked at using OVITO. Polyhedral template matching (PTM) analysis was used to determine the atomic structures. Stacking faults (SFs) were found based on HCP structure in the fcc phase. The onset of the Shockley partials and further the nucleation of SFs were correlated with the corresponding stresses. Finding the activated deformation systems, and therefore the Schmid factors, the critical resolved shear stresses for deformation twin nucleation were found for each GB and at each temperature.

For sigma 27, 77 K, 300K, and 600 K the simulation box showing the dislocations and SFs have been shown for three different stances, one from the elastic region, one from the yield region and one from the plastic region (Figure 35). Also, the GB has been zoomed in to show the nucleation of SFs and deformation twins and their systems (Figure 36). The results were similar for the other GBs and the results for all the GBs are shown in Table 9.

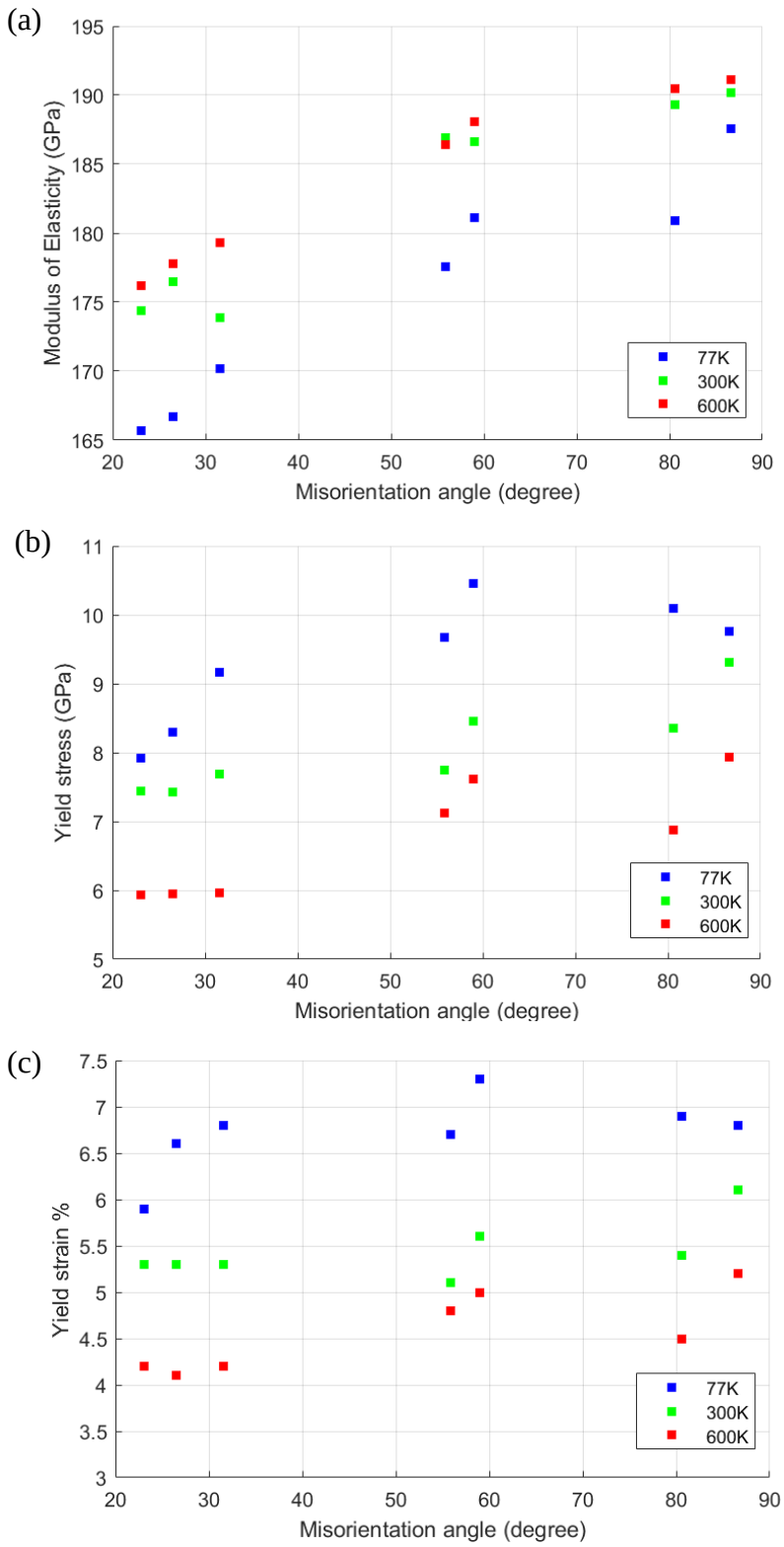

Figure 34. (a) Modulus of elasticity, (b) yield stress, and (c) yield strain % versus the GBs' misorientation angle at three different temperature.

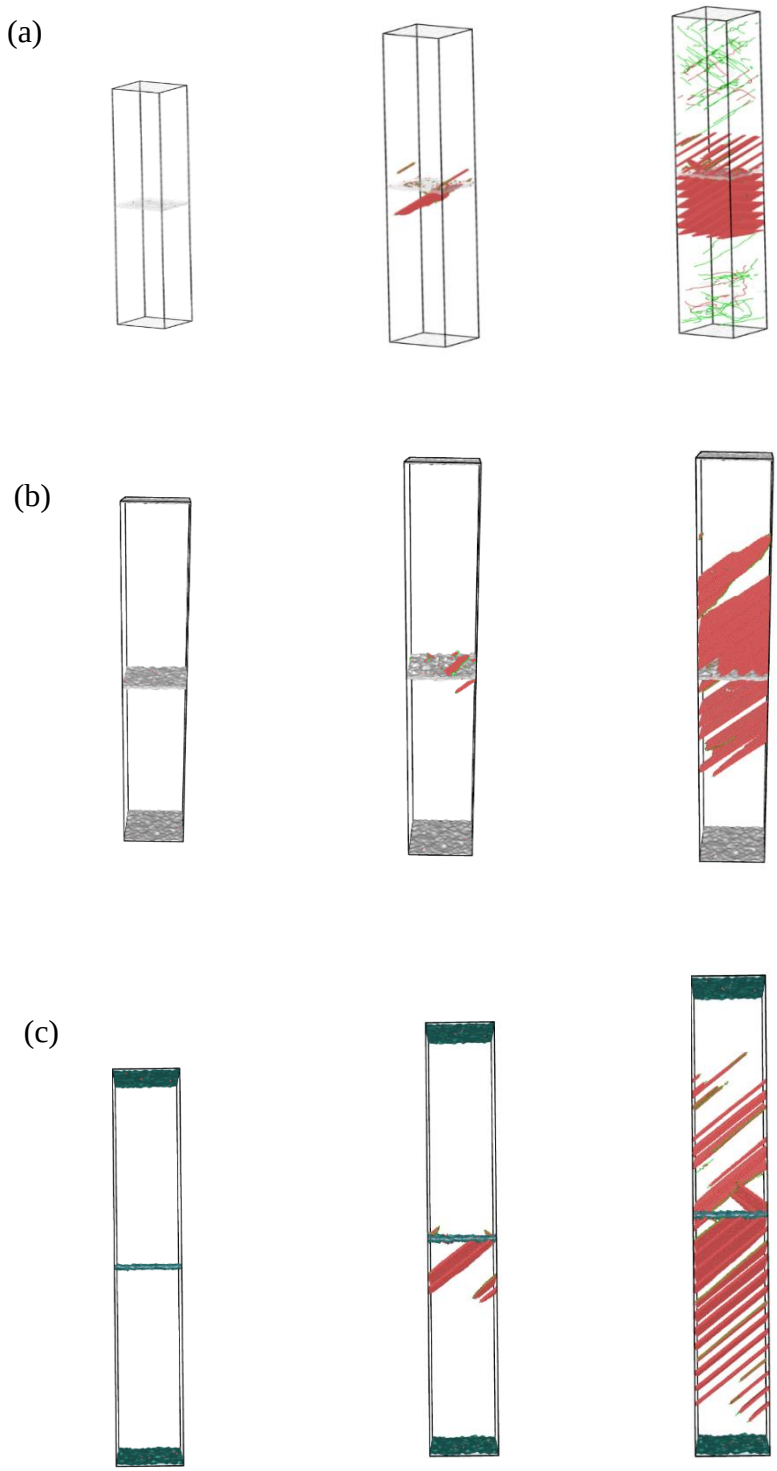

Figure 35. Simulation system during the tensile test, red color is associated with the deformation twins corresponding to the elastic region, the yield region, and the early plastic region for GB sigma 27 at (a) 77K, (b) 300K, and (c) 600K.

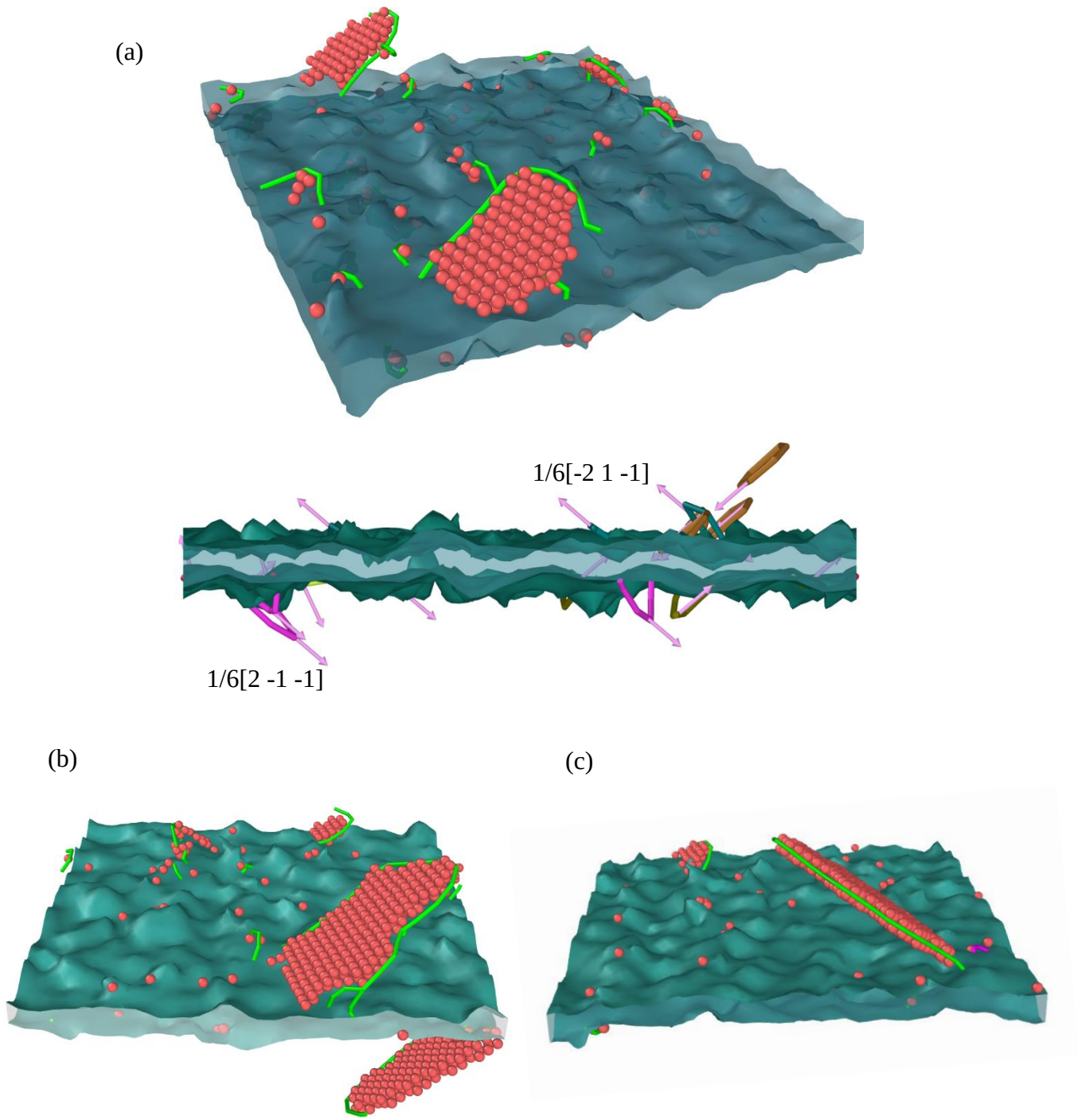

Figure 36. The grain boundary region is shown with the Shockley partial dislocation shown in green and the HCP phase shown in red on for GB 27 at (a) 77K, (b) 300K, and (c) 600K. The Burgers vectors of the activated systems is shown in light pink for 77K.

As seen in Figure 36 the Burgers vector of activated systems in the two grains of the bi-crystal is shown to be 1/6[2 -1 -1] and 1/6[-2 1 -1] which are both in the direction of twin systems in fcc crystals. For all the GBs studied, the Shockley partial dislocations started nucleating from the GBs. With the growth of the Shockley partials in the bulk crystal, stacking faults were left behind which eventually nucleated the deformation twins when the resolved shear stress reached the CRSS for twin.

Table 9. Critical resolved shear stress (CRSS) for twining for all the GBs and at all the temperatures for the uniaxial tensile test.

Sigma	**Misorientation Angle**	**Temperature [K]**	**Yield Strength [GPa]**	**CRSS for twin [GPa]**
27	31.6	77K	9.17	4.32
		77K, 2nd trial	9.08	4.28
		300K	7.69	3.62
		600K	5.96	2.80
19	26.53	77K	8.3	3.91
		300K	7.43	3.50
		600K	5.95	2.80
17	86.60	77K	9.76	4.60
		300K	9.31	4.39
		600K	7.94	3.74
51	23.07	77K	7.92	3.73
		300K	7.44	3.51
		600K	5.93	2.79
43	80.63	77K	10.10	4.76
		300K	8.35	3.94
		600K	6.87	3.24
41	55.88	77K	9.67	4.56
		300K	7.74	3.65
		600K	7.12	3.36
33	58.98	77K	10.45	4.93
		300K	8.46	3.99
		600K	7.62	3.59

The CRSS for twin was different for each of the bicrystals showing the effect of the GB type on the twin nucleation behavior at all the three temperatures tested. The Shockley partials and further the deformation twins nucleation near a combination of the four elements Co, Cr, Fe, and Ni, but the majority of them nucleated near the Cr-rich regions. Therefore, the elemental segregation of Cr at the GB facilitated the nucleation of the deformation twin and can be used as a guidance in segregation engineering.

6.4 Conclusions

The simulation results suggest that symmetric twist GB types affect the mechanical behavior and material properties of CoCrFeNi HEA at different temperature. Modulus of elasticity increased with the increase in the misorientation angle. No direct trend has been observed between the GB misorientation angles and the yield stress and strain in this alloy. With the increase in temperature the yield strength, yield strain, and CRSS for twinning decreased, and the modulus of elasticity increased. At temperature close to the melting point of the alloy, the softening effect is captured and decrease in modulus of elasticity was observed. MCMD chemical equilibrium simulations resulted in the GBs being Cr-rich and Ni- deficient Twin mostly nucleated from the Cr-rich regions and therefore doping the GB with Cr can positively affect the twin nucleation in this alloy although other considerations should be taken into account for instance the effect of on the GB corrosion behavior of this alloy.

CHAPTER SEVEN: SUMMARY AND CONCLUSIONS

In this research experimental and computational approaches are used to further identify the underlying plastic deformation mechanisms in HEAs giving rise to their improved properties. High resolution digital image correlation and electron backscatter diffraction have been used to find the dislocation slip critical resolved shear stress in $Al_{0.3}$CoCrFeNi polycrystalline under tension. The tensile yield strength was found to be 149.3 MPa and the modulus of elasticity was found to be 190 GPa. The tensile room temperature slip CRSS was found to be 63±2 MPa based on the activated slip system of (-1 1 1)[-1 -1 0] which also had the highest Schmid factor of 0.42.

Molecular dynamics and Monte Carlo molecular dynamics simulation have been used to identify the effect of different symmetric twist GB types and elemental segregation on deformation twins in CoCrFeNi bicrystals at three different temperatures 77 K, 100 K, and 300 K. Addition of Mn to CoCrFeNi HEA is detrimental to the yield and ultimate strength observed from experimental and molecular dynamics modeling. More twin nucleation and growth in CoCrFeMnNi caused it to be more ductile compared to CoCrFeNi when twinning nucleation and growth is accommodated. GB types affect the deformation twin behavior of the CoCrFeNi and CoCrFeMnNi HEAs.

The MCMD simulation results suggest that symmetric twist grain GB types affect the mechanical behavior and material properties of CoCrFeNi HEA at different temperature. No direct trend has been observed between the GB misorientation angles and the mechanical properties in this alloy. With the increase in temperature the yield strength, yield strain, and CRSS for twinning decreased, and the modulus of elasticity increased. At temperature close to the melting point of the alloy, the softening effect is captured and decrease in modulus of elasticity was observed. MCMD runs resulted in an increase in the Cr concentration and a decrease in the Ni concentration at the GBs.

The results of this research help to further understand the underlying micro and nano-scale phenomena of the improved properties observed in HEAs, identify the preferential grain boundaries for twin nucleation at different temperature. Therefore, metal alloys with even better properties can be designed and developed using GB engineering and elemental segregation engineering.

FUTURE WORK

Experimental

Further investigation of dislocation slip and deformation twinning nucleation and growth in fcc HEAs requires further electron microscopy on postmortem samples using transmission electron microscope (TEM). Although computationally the effects of temperature and GB type has been investigated in this research, experimentally further tensile tests at cryogenic temperature using HRDIC can further shed light into the twin nucleation preferential grain boundaries. Also, in order to exclude the effect of the existence of other grain on the deformation of each crystal and the CRSS for slip in the each of the crystals, single crystals of the alloy with different orientations can be used.

Properties of HEAs can further be improved by designing the alloy such that it shows both TWIP and transformation induced plasticity (TRIP) behavior. Metastable TWIP/TRIP HEAs can be designed by tuning the SFE. The TRIP and TWIP effects, their interaction with dislocation plasticity needs to be studied and specifically with respect to the effect of the microstructure of the alloy. Therefore, another path to further enrich the information on the grain and sub grain level plastic deformation mevhanisms in HEAs in order to reach to improved physics based plasticity models of these alloys and to design improved HEAs is to focus on TWIP/TRIP HEA.

Computational

Monte Carlo molecular dynamics (MCMD) can be further continued to ensure achieving chemical equilibrium in HEAs. Furthermore, the MCMD can be optimized using reinforcement learning techniques or machine learning techniques [142–145]. In MC the atoms are randomly chosen for swaps and therefore reaching the equilibrium/lowest possible energy is time consuming and computationally expensive. The choice of atoms being chosen for each swap can be modified at each step of the simulation based on the knowledge the system gains at each step [146]. Therefore, through reinforcement learning, MCMD simulation time can be reduced.

CHAPTER EIGHT: REFERENCES

[1] G. Laplanche, O. Horst, F. Otto, G. Eggeler, E.P. George, Microstructural evolution of a CoCrFeMnNi high-entropy alloy after swaging and annealing, J. Alloys Compd. 647 (2015) 548–557. doi:10.1016/j.jallcom.2015.05.129.

[2] F. Otto, Y. Yang, H. Bei, E.P. George, Relative effects of enthalpy and entropy on the phase stability of equiatomic high-entropy alloys, Acta Mater. (2013). doi:10.1016/j.actamat.2013.01.042.

[3] B. Gludovatz, A. Hohenwarter, K.V.S. Thurston, H. Bei, Z. Wu, E.P. George, R.O. Ritchie, Exceptional damage-tolerance of a medium-entropy alloy CrCoNi at cryogenic temperatures, Nat. Commun. (2016). doi:10.1038/ncomms10602.

[4] K.V.S. Thurston, B. Gludovatz, A. Hohenwarter, G. Laplanche, E.P. George, R.O. Ritchie, Effect of temperature on the fatigue-crack growth behavior of the high-entropy alloy CrMnFeCoNi, Intermetallics. (2017). doi:10.1016/j.intermet.2017.05.009.

[5] H. Torbati-Sarraf, M. Shabani, P.D. Jablonski, G.J. Pataky, A. Poursaee, The influence of incorporation of Mn on the pitting corrosion performance of CrFeCoNi High Entropy Alloy at different temperatures, Mater. Des. 184 (2019) 108170. doi:10.1016/J.MATDES.2019.108170.

[6] B. Cantor, I.T.H. Chang, P. Knight, A.J.B. Vincent, Microstructural development in equiatomic multicomponent alloys, Mater. Sci. Eng. A. (2004). doi:10.1016/j.msea.2003.10.257.

[7] J.W. Yeh, Recent progress in high-entropy alloys, Ann. Chim. Sci. Des Mater. 31 (2006) 633–648. doi:10.3166/acsm.31.633-648.

[8] D.B. Miracle, O.N. Senkov, A critical review of high entropy alloys and related concepts,

Acta Mater. 122 (2017) 448–511. doi:10.1016/j.actamat.2016.08.081.

[9] O.N. Senkov, G.B. Wilks, D.B. Miracle, C.P. Chuang, P.K. Liaw, Refractory high-entropy alloys, Intermetallics. (2010). doi:10.1016/j.intermet.2010.05.014.

[10] E.J. Pickering, N.G. Jones, High-entropy alloys: a critical assessment of their founding principles and future prospects, Int. Mater. Rev. (2016). doi:10.1080/09506608.2016.1180020.

[11] A. Gali, E.P. George, Tensile properties of high- and medium-entropy alloys, Intermetallics. (2013). doi:10.1016/j.intermet.2013.03.018.

[12] B. Gludovatz, A. Hohenwarter, D. Catoor, E.H. Chang, E.P. George, R.O. Ritchie, A fracture-resistant high-entropy alloy for cryogenic applications, Science (80-.). (2014). doi:10.1126/science.1254581.

[13] G. Laplanche, A. Kostka, O.M. Horst, G. Eggeler, E.P. George, Microstructure evolution and critical stress for twinning in the CrMnFeCoNi high-entropy alloy, Acta Mater. (2016). doi:10.1016/j.actamat.2016.07.038.

[14] D.B. Miracle, High-Entropy Alloys: A Current Evaluation of Founding Ideas and Core Effects and Exploring “Nonlinear Alloys,” JOM. (2017). doi:10.1007/s11837-017-2527-z.

[15] C.P. Lee, C.C. Chang, Y.Y. Chen, J.W. Yeh, H.C. Shih, Effect of the aluminium content of AlxCrFe1.5MnNi0.5 high-entropy alloys on the corrosion behaviour in aqueous environments, Corros. Sci. (2008). doi:10.1016/j.corsci.2008.04.011.

[16] D. Li, Y. Zhang, The ultrahigh charpy impact toughness of forged AlxCoCrFeNi high entropy alloys at room and cryogenic temperatures, Intermetallics. (2016). doi:10.1016/j.intermet.2015.11.002.

[17] M.H. Chuang, M.H. Tsai, W.R. Wang, S.J. Lin, J.W. Yeh, Microstructure and wear

behavior of AlxCo 1.5CrFeNi1.5Tiy high-entropy alloys, Acta Mater. 59 (2011) 6308–6317. doi:10.1016/j.actamat.2011.06.041.

[18] D. Li, M.C. Gao, J.A. Hawk, Y. Zhang, Annealing effect for the Al0.3CoCrFeNi high-entropy alloy fibers, J. Alloys Compd. (2019). doi:10.1016/j.jallcom.2018.11.116.

[19] M. Shabani, J. Indeck, K. Hazeli, P.D. Jablonski, G.J. Pataky, Effect of Strain Rate on the Tensile Behavior of CoCrFeNi and CoCrFeMnNi High-Entropy Alloys, J. Mater. Eng. Perform. (2019). doi:10.1007/s11665-019-04176-y.

[20] J.J. Licavoli, M.C. Gao, J.S. Sears, P.D. Jablonski, J.A. Hawk, Microstructure and Mechanical Behavior of High-Entropy Alloys, J. Mater. Eng. Perform. (2015). doi:10.1007/s11665-015-1679-7.

[21] K. Biswas, J.W. Yeh, P.P. Bhattacharjee, J.T.M. DeHosson, High entropy alloys: Key issues under passionate debate, Scr. Mater. (2020). doi:10.1016/j.scriptamat.2020.07.010.

[22] J.W. Yeh, S.K. Chen, S.J. Lin, J.Y. Gan, T.S. Chin, T.T. Shun, C.H. Tsau, S.Y. Chang, Nanostructured high-entropy alloys with multiple principal elements: Novel alloy design concepts and outcomes, Adv. Eng. Mater. (2004). doi:10.1002/adem.200300567.

[23] Y. Zhang, S. Guo, C.T. Liu, X. Yang, Phase formation rules, in: High-Entropy Alloy. Fundam. Appl., 2016. doi:10.1007/978-3-319-27013-5_2.

[24] Y. Zhang, Y.J. Zhou, J.P. Lin, G.L. Chen, P.K. Liaw, Solid-solution phase formation rules for multi-component alloys, Adv. Eng. Mater. (2008). doi:10.1002/adem.200700240.

[25] M. Schütze, Materials sciences and technology - A comprehensive treatment. Hrsg. von R. W. Cahn, P. Hassen, E. J. Kramer, VCH-Verlagsgesellschaft mbH, Weinheim 1996 Bände 8, 17A und 17B. Vol. 8, DM 498,00, ISBN 3-527-26821-9, Vol. 17A/B - DM 380,00, ISBN 3 - 527 -268, Mater. Corros. Und Korrosion. (1996).

doi:10.1002/maco.19960470909.

[26] F.R.N. Nabarro, The mechanical properties of metallic solid solutions, Proc. Phys. Soc. (1946). doi:10.1088/0959-5309/58/6/305.

[27] M.H. Tsai, J.W. Yeh, High-entropy alloys: A critical review, Mater. Res. Lett. (2014). doi:10.1080/21663831.2014.912690.

[28] S. V. Divinski, A. V. Pokoev, N. Esakkiraja, A. Paul, A Mystery of "Sluggish Diffusion" in High-Entropy Alloys: The Truth or a Myth?, Diffus. Found. (2018). doi:10.4028/www.scientific.net/df.17.69.

[29] S. Ranganathan, Alloyed pleasures: Multimetallic cocktails, Curr. Sci. (2003).

[30] E.P. George, W.A. Curtin, C.C. Tasan, High entropy alloys: A focused review of mechanical properties and deformation mechanisms, Acta Mater. (2020). doi:10.1016/j.actamat.2019.12.015.

[31] H.Y. Diao, R. Feng, K.A. Dahmen, P.K. Liaw, Fundamental deformation behavior in high-entropy alloys: An overview, Curr. Opin. Solid State Mater. Sci. (2017). doi:10.1016/j.cossms.2017.08.003.

[32] S. Picak, J. Liu, C. Hayrettin, W. Nasim, D. Canadinc, K. Xie, Y.I. Chumlyakov, I. V. Kireeva, I. Karaman, Anomalous work hardening behavior of Fe40Mn40Cr10Co10 high entropy alloy single crystals deformed by twinning and slip, Acta Mater. (2019). doi:10.1016/j.actamat.2019.09.048.

[33] B. Uzer, S. Picak, J. Liu, T. Jozaghi, D. Canadinc, I. Karaman, Y.I. Chumlyakov, I. Kireeva, On the mechanical response and microstructure evolution of NiCoCr single crystalline medium entropy alloys, Mater. Res. Lett. (2018). doi:10.1080/21663831.2018.1478331.

[34] S. Huang, H. Huang, W. Li, D. Kim, S. Lu, X. Li, E. Holmström, S.K. Kwon, L. Vitos, Twinning in metastable high-entropy alloys, Nat. Commun. (2018). doi:10.1038/s41467-018-04780-x.

[35] M. Jo, Y.M. Koo, B.J. Lee, B. Johansson, L. Vitos, S.K. Kwon, Theory for plasticity of face-centered cubic metals, Proc. Natl. Acad. Sci. U. S. A. (2014). doi:10.1073/pnas.1400786111.

[36] S.L. Shang, W.Y. Wang, B.C. Zhou, Y. Wang, K.A. Darling, L.J. Kecskes, S.N. Mathaudhu, Z.K. Liu, Generalized stacking fault energy, ideal strength and twinnability of dilute Mg-based alloys: A first-principles study of shear deformation, Acta Mater. (2014). doi:10.1016/j.actamat.2013.12.019.

[37] S. Huang, W. Li, E. Holmström, S.K. Kwon, O. Eriksson, L. Vitos, Plastic deformation transition in FeCrCoNiAlx high-entropy alloys, Mater. Res. Lett. (2019). doi:10.1080/21663831.2019.1644683.

[38] S.J. Sun, Y.Z. Tian, H.R. Lin, H.J. Yang, X.G. Dong, Y.H. Wang, Z.F. Zhang, Transition of twinning behavior in CoCrFeMnNi high entropy alloy with grain refinement, Mater. Sci. Eng. A. (2018). doi:10.1016/j.msea.2017.12.022.

[39] I. Gutierrez-Urrutia, D. Raabe, Grain size effect on strain hardening in twinning-induced plasticity steels, Scr. Mater. (2012). doi:10.1016/j.scriptamat.2012.01.037.

[40] S.F. Liu, Y. Wu, H.T. Wang, J.Y. He, J.B. Liu, C.X. Chen, X.J. Liu, H. Wang, Z.P. Lu, Stacking fault energy of face-centered-cubic high entropy alloys, Intermetallics. (2018). doi:10.1016/j.intermet.2017.10.004.

[41] M.J. Mills, T. Neeraj, Dislocations in Metals and Metallic Alloys, in: Encycl. Mater. Sci. Technol., 2001. doi:10.1016/b0-08-043152-6/00406-x.

[42] W.T. Read, Dislocations, Phys. Today. (1953). doi:10.1063/1.3061039.

[43] D. Hull, D.J. Bacon, Introduction to Dislocations, 2011. doi:10.1016/C2009-0-64358-0.

[44] J. Wang, H. Sehitoglu, H.J. Maier, Dislocation slip stress prediction in shape memory alloys, Int. J. Plast. (2014). doi:10.1016/j.ijplas.2013.08.017.

[45] G.E. Dieter, D. Bacon, S.M. Copley, C. a Wert, G.L. Wilkes, Mechanical Metallurgy, 1988. doi:10.1111/nep.12265.

[46] W. Callister, D. Rethwisch, Materials science and engineering: an introduction, 2007. doi:10.1016/0025-5416(87)90343-0.

[47] D. Hull, D.J. Bacon, Dislocations in Face-centered Cubic Metals, in: Introd. to Dislocations, 2011. doi:10.1016/b978-0-08-096672-4.00005-0.

[48] S. Mahajan, D.F. Williams, Deformation Twinning in Metals and Alloys, Int. Metall. Rev. (1973). doi:10.1179/imtlr.1973.18.2.43.

[49] J.W. Christian, S. Mahajan, Deformation twinning, Prog. Mater. Sci. (1995). doi:10.1016/0079-6425(94)00007-7.

[50] M. Chen, E. Ma, K.J. Hemker, H. Sheng, Y. Wang, X. Cheng, Deformation twinning in nanocrystalline aluminum, Science (80-.). (2003). doi:10.1126/science.1083727.

[51] S. Mahajan, G.Y. Chin, Twin-slip, twin-twin and slip-twin interactions in Co-8 wt.% Fe alloy single crystals, Acta Metall. (1973). doi:10.1016/0001-6160(73)90059-X.

[52] S. Mahajan, C.S. Pande, M.A. Imam, B.B. Rath, Formation of annealing twins in f.c.c. crystals, Acta Mater. (1997). doi:10.1016/S1359-6454(96)00336-9.

[53] S.W. Wu, G. Wang, J. Yi, Y.D. Jia, I. Hussain, Q.J. Zhai, P.K. Liaw, Strong grain-size effect on deformation twinning of an Al0.1CoCrFeNi high-entropy alloy, Mater. Res. Lett. (2017). doi:10.1080/21663831.2016.1257514.

[54] F. Otto, A. Dlouhý, C. Somsen, H. Bei, G. Eggeler, E.P. George, The influences of temperature and microstructure on the tensile properties of a CoCrFeMnNi high-entropy alloy, Acta Mater. (2013). doi:10.1016/j.actamat.2013.06.018.

[55] Y. Wang, B. Liu, K. Yan, M. Wang, S. Kabra, Y.L. Chiu, D. Dye, P.D. Lee, Y. Liu, B. Cai, Probing deformation mechanisms of a FeCoCrNi high-entropy alloy at 293 and 77 K using in situ neutron diffraction, Acta Mater. 154 (2018) 79–89. doi:10.1016/j.actamat.2018.05.013.

[56] Z.C. Cordero, B.E. Knight, C.A. Schuh, Six decades of the Hall–Petch effect – a survey of grain-size strengthening studies on pure metals, Int. Mater. Rev. (2016). doi:10.1080/09506608.2016.1191808.

[57] N.J. Petch, The cleavage strength of polycrystals, J. Iron Steel InstInst. (1953).

[58] E.O. Hall, The deformation and ageing of mild steel: III Discussion of results, Proc. Phys. Soc. Sect. B. (1951). doi:10.1088/0370-1301/64/9/303.

[59] Y. Deng, C.C. Tasan, K.G. Pradeep, H. Springer, A. Kostka, D. Raabe, Design of a twinning-induced plasticity high entropy alloy, Acta Mater. (2015). doi:10.1016/j.actamat.2015.04.014.

[60] J. Lu, L. Hultman, E. Holmström, K.H. Antonsson, M. Grehk, W. Li, L. Vitos, A. Golpayegani, Stacking fault energies in austenitic stainless steels, Acta Mater. (2016). doi:10.1016/j.actamat.2016.03.042.

[61] B. Qin, H.K.D.H. Bhadeshia, Plastic strain due to twinning in austenitic TWIP steels, Mater. Sci. Technol. (2008). doi:10.1179/174328408X263688.

[62] O. Grässel, L. Krüger, G. Frommeyer, L.W. Meyer, High strength Fe-Mn-(Al, Si) TRIP/TWIP steels development - properties - application, Int. J. Plast. (2000).

doi:10.1016/S0749-6419(00)00015-2.

[63] D.T. Pierce, J.A. Jiménez, J. Bentley, D. Raabe, J.E. Wittig, The influence of stacking fault energy on the microstructural and strain-hardening evolution of Fe-Mn-Al-Si steels during tensile deformation, Acta Mater. 100 (2015) 178–190. doi:10.1016/j.actamat.2015.08.030.

[64] D. Raabe, Z. Li, D. Ponge, Metastability alloy design, MRS Bull. (2019). doi:10.1557/mrs.2019.72.

[65] L. Rémy, A. Pineau, Twinning and strain-induced f.c.c. → h.c.p. transformation on the mechanical properties of CoNiCrMo alloys, Mater. Sci. Eng. (1976). doi:10.1016/0025-5416(76)90234-2.

[66] G. Laplanche, A. Kostka, O.M. Horst, G. Eggeler, E.P. George, Microstructure evolution and critical stress for twinning in the CrMnFeCoNi high-entropy alloy, Acta Mater. (2016). doi:10.1016/j.actamat.2016.07.038.

[67] O. Bouaziz, S. Allain, C. Scott, Effect of grain and twin boundaries on the hardening mechanisms of twinning-induced plasticity steels, Scr. Mater. (2008). doi:10.1016/j.scriptamat.2007.10.050.

[68] W.Z. Han, Z.F. Zhang, S.D. Wu, S.X. Li, Combined effects of crystallographic orientation, stacking fault energy and grain size on deformation twinning in fcc crystals, Philos. Mag. (2008). doi:10.1080/14786430802438168.

[69] W.M. Choi, Y.H. Jo, S.S. Sohn, S. Lee, B.J. Lee, Understanding the physical metallurgy of the CoCrFeMnNi high-entropy alloy: An atomistic simulation study, Npj Comput. Mater. (2018). doi:10.1038/s41524-017-0060-9.

[70] Z. Li, S. Zhao, R.O. Ritchie, M.A. Meyers, Mechanical properties of high-entropy alloys

with emphasis on face-centered cubic alloys, Prog. Mater. Sci. (2019). doi:10.1016/j.pmatsci.2018.12.003.

[71] S. Alkan, A. Ojha, H. Sehitoglu, Determination of latent hardening response for FeNiCoCrMn for twin-twin interactions, Acta Mater. (2018). doi:10.1016/j.actamat.2017.12.058.

[72] P. Reu, All about speckles: Speckle size measurement, Exp. Tech. (2014). doi:10.1111/ext.12110.

[73] R. Bigger, B. Blaysat, C. Boo, M. Grewer, J. Hu, A. Jones, M. Klein, K. Raghavan, P. Reu, T. Schmidt, T. Siebert, M. Simenson, D. Turner, A. Vieira, T. Weikert, A Good Practices Guide for Digital Image Correlation, Int. Digit. Image Correl. Soc. (2018).

[74] M.A. Sutton, J.J. Orteu, H.W. Schreier, Image correlation for shape, motion and deformation measurements, Springer, 2009.

[75] H. Schreier, J.J. Orteu, M.A. Sutton, Image correlation for shape, motion and deformation measurements: Basic concepts, theory and applications, 2009. doi:10.1007/978-0-387-78747-3.

[76] C. Ni, Scanning Electron Microscopy (SEM), in: Encycl. Tribol., 2013. doi:10.1007/978-0-387-92897-5_1217.

[77] T. Kogure, Electron Microscopy, in: Dev. Clay Sci., 2013. doi:10.1016/B978-0-08-098259-5.00011-1.

[78] D.B. Williams, C.B. Carter, Transmission electron microscopy: A textbook for materials science, 2009. doi:10.1007/978-0-387-76501-3.

[79] G.H. Michler, W. Lebek, Electron microscopy of polymers, in: Polym. Morphol. Princ. Charact. Process., 2016. doi:10.1002/9781118892756.ch3.

[80] S. Yesilkir-Baydar, O.N. Oztel, R. Cakir-Koc, A. Candayan, Evaluation techniques, in: Nanobiomaterials Sci. Dev. Eval., 2017. doi:10.1016/B978-0-08-100963-5.00011-2.

[81] J. Rose, Characterization of Nanomaterials in Complex Environmental and Biological Media, Front. Nanosci. (2015).

[82] A.J. Schwartz, M. Kumar, B.L. Adams, D.P. Field, Electron backscatter diffraction in materials science, 2009. doi:10.1007/978-0-387-88136-2.

[83] Y.J. Chen, J. Hjelen, H.J. Roven, Application of EBSD technique to ultrafine grained and nanostructured materials processed by severe plastic deformation: Sample preparation, parameters optimization and analysis, Trans. Nonferrous Met. Soc. China (English Ed. (2012). doi:10.1016/S1003-6326(11)61390-3.

[84] F.J. Humphreys, Grain and subgrain characterisation by electron backscatter diffraction, J. Mater. Sci. (2001). doi:10.1023/A:1017973432592.

[85] O. Instruments, Oxford Instruments, Optimizing SEM Condition, EBSD.Com. (2017).

[86] T.B. Britton, J. Jiang, Y. Guo, A. Vilalta-Clemente, D. Wallis, L.N. Hansen, A. Winkelmann, A.J. Wilkinson, Tutorial: Crystal orientations and EBSD - Or which way is up?, Mater. Charact. 117 (2016) 113–126. doi:10.1016/j.matchar.2016.04.008.

[87] E.P. George, D. Raabe, R.O. Ritchie, High-entropy alloys, Nat. Rev. Mater. 4 (2019) 515–534. doi:10.1038/s41578-019-0121-4.

[88] M.A. Hemphill, T. Yuan, G.Y. Wang, J.W. Yeh, C.W. Tsai, A. Chuang, P.K. Liaw, Fatigue behavior of Al0.5CoCrCuFeNi high entropy alloys, Acta Mater. (2012). doi:10.1016/j.actamat.2012.06.046.

[89] B. Gwalani, S. Gorsse, D. Choudhuri, Y. Zheng, R.S. Mishra, R. Banerjee, Tensile yield strength of a single bulk Al 0.3 CoCrFeNi high entropy alloy can be tuned from 160 MPa

to 1800 MPa, Scr. Mater. (2019). doi:10.1016/j.scriptamat.2018.10.023.

[90] U. Roy, H. Roy, H. Daoud, U. Glatzel, K.K. Ray, Fracture toughness and fracture micromechanism in a cast AlCoCrCuFeNi high entropy alloy system, Mater. Lett. (2014). doi:10.1016/j.matlet.2014.06.067.

[91] T.T. Shun, Y.C. Du, Microstructure and tensile behaviors of FCC Al0.3CoCrFeNi high entropy alloy, J. Alloys Compd. (2009). doi:10.1016/j.jallcom.2008.12.088.

[92] K. Liu, M. Komarasamy, B. Gwalani, S. Shukla, R.S. Mishra, Fatigue behavior of ultrafine grained triplex Al0.3CoCrFeNi high entropy alloy, Scr. Mater. (2019). doi:10.1016/j.scriptamat.2018.08.048.

[93] I. V. Kireeva, Y.I. Chumlyakov, Z. V. Pobedennaya, A. V. Vyrodova, I. V. Kuksgauzen, V. V. Poklonov, D.A. Kuksgauzen, The orientation dependence of critical shear stresses in Al0.3CoCrFeNi high-entropy alloy single crystals, Tech. Phys. Lett. (2017). doi:10.1134/S1063785017070082.

[94] I. V. Kireeva, Y.I. Chumlyakov, Z. V. Pobedennaya, I. V. Kuksgausen, I. Karaman, Orientation dependence of twinning in single crystalline CoCrFeMnNi high-entropy alloy, Mater. Sci. Eng. A. (2017). doi:10.1016/j.msea.2017.08.065.

[95] M. Kuczyk, L. Kotte, J. Kaspar, M. Zimmermann, C. Leyens, Alloy Design and Microstructure Evolution in the AlxCoCrFeNi Alloy System Synthesized by Laser Metal Deposition, Front. Mater. (2020). doi:10.3389/fmats.2020.00242.

[96] W.R. Wang, W.L. Wang, S.C. Wang, Y.C. Tsai, C.H. Lai, J.W. Yeh, Effects of Al addition on the microstructure and mechanical property of Al xCoCrFeNi high-entropy alloys, Intermetallics. (2012). doi:10.1016/j.intermet.2012.03.005.

[97] C. Wang, C.L. Tracy, S. Park, J. Liu, F. Ke, F. Zhang, T. Yang, S. Xia, C. Li, Y. Wang, Y.

Zhang, W.L. Mao, R.C. Ewing, Phase transformations of Al-bearing high-entropy alloys AlxCoCrFeNi (x = 0, 0.1, 0.3, 0.75, 1.5) at high pressure, Appl. Phys. Lett. (2019). doi:10.1063/1.5079868.

[98] L. Patriarca, A. Ojha, H. Sehitoglu, Y.I. Chumlyakov, Slip nucleation in single crystal FeNiCoCrMn high entropy alloy, Scr. Mater. (2016). doi:10.1016/j.scriptamat.2015.09.009.

[99] W. Abuzaid, H. Sehitoglu, Critical resolved shear stress for slip and twin nucleation in single crystalline FeNiCoCrMn high entropy alloy, Mater. Charact. (2017). doi:10.1016/j.matchar.2017.05.014.

[100] N.L. Okamoto, S. Fujimoto, Y. Kambara, M. Kawamura, Z.M.T. Chen, H. Matsunoshita, K. Tanaka, H. Inui, E.P. George, Size effect, critical resolved shear stress, stacking fault energy, and solid solution strengthening in the CrMnFeCoNi high-entropy alloy, Sci. Rep. (2016). doi:10.1038/srep35863.

[101] G.J. Pataky, H. Sehitoglu, Experimental Methodology for Studying Strain Heterogeneity with Microstructural Data from High Temperature Deformation, Exp. Mech. (2015). doi:10.1007/s11340-014-9926-7.

[102] G.E. Totten, L. Xie, K. Funatani, Handbook of Mechanical Alloy Design, 2003. doi:10.1201/9780203913307.

[103] T.R. Bieler, P. Eisenlohr, C. Zhang, H.J. Phukan, M.A. Crimp, Grain boundaries and interfaces in slip transfer, Curr. Opin. Solid State Mater. Sci. (2014). doi:10.1016/j.cossms.2014.05.003.

[104] W.J. Poole, J.D. Embury, D.J. Lloyd, Work hardening in aluminium alloys, in: Fundam. Alum. Metall. Prod. Process. Appl., 2010. doi:10.1533/9780857090256.2.307.

[105] B. López, J.M. Rodriguez-Ibabe, Recrystallisation and grain growth in hot working of steels, in: Microstruct. Evol. Met. Form. Process., 2012. doi:10.1016/B978-0-85709-074-4.50004-1.

[106] Q. Jiao, G.D. Sim, M. Komarasamy, R.S. Mishra, P.K. Liaw, J.A. El-Awady, Thermo-mechanical response of single-phase face-centered-cubic AlxCoCrFeNi high-entropy alloy microcrystals, Mater. Res. Lett. (2018). doi:10.1080/21663831.2018.1446468.

[107] J.G. Lee, Computational materials science : an introduction, 2004.

[108] A. Heinecke, W. Eckhardt, M. Horsch, H.J. Bungartz, Molecular dynamics simulation, in: SpringerBriefs Comput. Sci., 2015. doi:10.1007/978-3-319-17148-7_2.

[109] Y. JUNG, Introduction to a Molecular Dynamics Simulation, Phys. High Technol. (2012). doi:10.3938/phit.21.037.

[110] M. Widom, W.P. Huhn, S. Maiti, W. Steurer, Hybrid Monte Carlo/molecular dynamics simulation of a refractory metal high entropy alloy, in: Metall. Mater. Trans. A Phys. Metall. Mater. Sci., 2014. doi:10.1007/s11661-013-2000-8.

[111] E.C. Neyts, A. Bogaerts, Combining molecular dynamics with monte carlo simulations: Implementations and applications, Theor. Chem. Acc. (2013). doi:10.1007/s00214-012-1320-x.

[112] B. Sadigh, P. Erhart, A. Stukowski, A. Caro, E. Martinez, L. Zepeda-Ruiz, Scalable parallel Monte Carlo algorithm for atomistic simulations of precipitation in alloys, Phys. Rev. B - Condens. Matter Mater. Phys. (2012). doi:10.1103/PhysRevB.85.184203.

[113] S.M. Rassoulinejad-Mousavi, Y. Zhang, Interatomic Potentials Transferability for Molecular Simulations: A Comparative Study for Platinum, Gold and Silver, Sci. Rep. (2018). doi:10.1038/s41598-018-20375-4.

[114] Q. Mao, A Molecular Dynamics Study of the Cellulose-Graphene Oxide Nanocomposites : The Interface Effects, 2018.

[115] P.H. Hünenberger, Thermostat algorithms for molecular dynamics simulations, Adv. Polym. Sci. (2005). doi:10.1007/b99427.

[116] M. Mecke, J. Winkelmann, J. Fischer, Molecular dynamics simulation of the liquid-vapor interface: The Lennard-Jones fluid, J. Chem. Phys. (1997). doi:10.1063/1.475217.

[117] A.J. Zaddach, C. Niu, C.C. Koch, D.L. Irving, Mechanical properties and stacking fault energies of NiFeCrCoMn high-entropy alloy, JOM. (2013). doi:10.1007/s11837-013-0771-4.

[118] J.M. Park, J. Moon, J.W. Bae, M.J. Jang, J. Park, S. Lee, H.S. Kim, Strain rate effects of dynamic compressive deformation on mechanical properties and microstructure of CoCrFeMnNi high-entropy alloy, Mater. Sci. Eng. A. (2018). doi:10.1016/j.msea.2018.02.031.

[119] D.L. Olmsted, S.M. Foiles, E.A. Holm, Survey of computed grain boundary properties in face-centered cubic metals: I. Grain boundary energy, Acta Mater. (2009). doi:10.1016/j.actamat.2009.04.007.

[120] S. Plimpton, Fast parallel algorithms for short-range molecular dynamics, J. Comput. Phys. (1995). doi:10.1006/jcph.1995.1039.

[121] A. Stukowski, Visualization and analysis of atomistic simulation data with OVITO-the Open Visualization Tool, Model. Simul. Mater. Sci. Eng. (2010). doi:10.1088/0965-0393/18/1/015012.

[122] Y. Mishin, D. Farkas, Atomistic simulation of [001] symmetrical tilt grain boundaries in NiAl, Philos. Mag. A Phys. Condens. Matter, Struct. Defects Mech. Prop. (1998).

doi:10.1080/014186198253679.

[123] A. Suzuki, Y. Mishin, Atomistic modeling of point defects and diffusion in copper grain boundaries, Interface Sci. (2003). doi:10.1023/A:1021599310093.

[124] W. Shinoda, M. Shiga, M. Mikami, Rapid estimation of elastic constants by molecular dynamics simulation under constant stress, Phys. Rev. B - Condens. Matter Mater. Phys. (2004). doi:10.1103/PhysRevB.69.134103.

[125] G.J. Martyna, D.J. Tobias, M.L. Klein, Constant pressure molecular dynamics algorithms, J. Chem. Phys. (1994). doi:10.1063/1.467468.

[126] M. Parrinello, A. Rahman, Polymorphic transitions in single crystals: A new molecular dynamics method, J. Appl. Phys. (1981). doi:10.1063/1.328693.

[127] M.E. Tuckerman, J. Alejandre, R. López-Rendón, A.L. Jochim, G.J. Martyna, A Liouville-operator derived measure-preserving integrator for molecular dynamics simulations in the isothermal-isobaric ensemble, J. Phys. A. Math. Gen. (2006). doi:10.1088/0305-4470/39/19/S18.

[128] A. Dullweber, B. Leimkuhler, R. McLachlan, Symplectic splitting methods for rigid body molecular dynamics, J. Chem. Phys. (1997). doi:10.1063/1.474310.

[129] A.P. Thompson, S.J. Plimpton, W. Mattson, General formulation of pressure and stress tensor for arbitrary many-body interaction potentials under periodic boundary conditions, J. Chem. Phys. (2009). doi:10.1063/1.3245303.

[130] B.G. Levine, J.E. Stone, A. Kohlmeyer, Fast analysis of molecular dynamics trajectories with graphics processing units-Radial distribution function histogramming, J. Comput. Phys. (2011). doi:10.1016/j.jcp.2011.01.048.

[131] M. Shabanisamghabady, Effect of Strain Rate on the Tensile Behavior of CoCrFeNi and

CoCrFeMnNi High Entropy Alloys, 2018.

[132] M. Kang, J.W. Won, K.R. Lim, H.J. Kwon, S.M. Seo, Y.S. Na, Compositional approach to designing Fcc high-entropy alloys that have an enlarged equiaxed zone, Metals (Basel). (2018). doi:10.3390/met8010054.

[133] A. Kwiatkowski da Silva, R.D. Kamachali, D. Ponge, B. Gault, J. Neugebauer, D. Raabe, Thermodynamics of grain boundary segregation, interfacial spinodal and their relevance for nucleation during solid-solid phase transitions, Acta Mater. (2019). doi:10.1016/j.actamat.2019.02.005.

[134] D. Raabe, S. Sandlöbes, J. Millán, D. Ponge, H. Assadi, M. Herbig, P.P. Choi, Segregation engineering enables nanoscale martensite to austenite phase transformation at grain boundaries: A pathway to ductile martensite, Acta Mater. (2013). doi:10.1016/j.actamat.2013.06.055.

[135] S. Mandal, K.G. Pradeep, S. Zaefferer, D. Raabe, A novel approach to measure grain boundary segregation in bulk polycrystalline materials in dependence of the boundaries' five rotational degrees of freedom, Scr. Mater. (2014). doi:10.1016/j.scriptamat.2014.02.016.

[136] K.G. Pradeep, N. Wanderka, P. Choi, J. Banhart, B.S. Murty, D. Raabe, Atomic-scale compositional characterization of a nanocrystalline AlCrCuFeNiZn high-entropy alloy using atom probe tomography, Acta Mater. (2013). doi:10.1016/j.actamat.2013.04.059.

[137] T. Frolov, W. Setyawan, R.J. Kurtz, J. Marian, A.R. Oganov, R.E. Rudd, Q. Zhu, Grain boundary phases in bcc metals, Nanoscale. (2018). doi:10.1039/c8nr00271a.

[138] Q. Zhu, A. Samanta, B. Li, R.E. Rudd, T. Frolov, Predicting phase behavior of grain boundaries with evolutionary search and machine learning, Nat. Commun. (2018).

doi:10.1038/s41467-018-02937-2.

[139] P. Wynblatt, D. Chatain, Modeling grain boundary and surface segregation in multicomponent high-entropy alloys, Phys. Rev. Mater. (2019). doi:10.1103/PhysRevMaterials.3.054004.

[140] P.J.E. Forsyth, R. King, G.J. Metcalfe, B. Chalmers, Grain boundaries in metals [7], Nature. (1946). doi:10.1038/158875a0.

[141] M.A. Gutierrez, G.D. Rodriguez, G. Bozzolo, H.O. Mosca, Melting temperature of CoCrFeNiMn high-entropy alloys, Comput. Mater. Sci. (2018). doi:10.1016/j.commatsci.2018.02.032.

[142] S. Karimi, A. Vahidi, Receding Horizon Motion Planning for Automated Lane Change and Merge Using Monte Carlo Tree Search and Level-K Game Theory, in: Proc. Am. Control Conf., 2020. doi:10.23919/ACC45564.2020.9147369.

[143] E. Sadrfaridpour, T. Razzaghi, I. Safro, Engineering fast multilevel support vector machines, Mach. Learn. (2019). doi:10.1007/s10994-019-05800-7.

[144] T. Razzaghi, I. Safro, J. Ewing, E. Sadrfaridpour, J.D. Scott, Predictive models for bariatric surgery risks with imbalanced medical datasets, Ann. Oper. Res. (2019). doi:10.1007/s10479-019-03156-8.

[145] E. Sadrfaridpour, S. Jeereddy, K. Kennedy, A. Luckow, T. Razzaghi, I. Safro, Algebraic multigrid support vector machines, in: ESANN 2017 - Proceedings, 25th Eur. Symp. Artif. Neural Networks, Comput. Intell. Mach. Learn., 2017.

[146] R.S. Sutton, A.G. Barto, Reinforcement Learning: An Introduction, IEEE Trans. Neural Networks. (1998). doi:10.1109/tnn.1998.712192.

Appendix A: LAMMPS Codes

Relaxation

```
################################################
# initialize
################################################

units metal
dimension 3
boundary p p p
atom_style atomic
atom_modify map array

# read in input file
read_data       hea1.data

mass    1 55.85
mass    2 58.69
mass    3 52.00
mass    4 58.93
mass    5 54.94

################################################
# Potential file
################################################
pair_style meam/c
pair_coeff * * library.meam Co Ni Cr Fe Mn hea.meam Fe Ni Cr Co Mn

neighbor 2.0 bin
neigh_modify delay 10 check yes
variable Tdesird equal 77.0
variable   Nsteps equal 300000
variable DumpFreq equal 3000

reset_timestep 0

thermo         100
thermo_style  custom step temp pe etotal pxx pyy pzz pxy pxz pyz press
lx ly lz
velocity all create ${Tdesird} 95812384
fix 3 all npt temp ${Tdesird} ${Tdesird} 1.0 aniso 0.0 0.0 1.0

dump mydump all atom ${DumpFreq}AnnealOut_*.dump
dump_modify mydump sort id

run ${Nsteps}
```

```
unfix 3

print "Print restart"
write_restart HEA_thermal_equilibrate.restart
```

Mechanical Testing

```
# Mechanical Tensile Test September 2020

################################################
# Initializing
################################################

units metal #units style is selected to be metal
# For style metal these are dt = 0.001 picoseconds,skin = 2.0 Angstroms
dimension 3 #running 3D simulation which is LAMMPS default
boundary p p p #xyz boundaries are set to be periodic
atom_style atomic
atom_modify map array

################################################
# Create System
################################################

#read in restart file which is from the MCMD step
read_restart       HEA_MC_882000.restart

mass    1 55.85 #Iron
mass    2 58.69 #Nickel
mass    3 52.00 #Chromium
mass    4 58.93 #Cobalt
mass    5 54.94 #Mangenese

################################################
# Potential file
################################################

pair_style meam/c #modified embedded-atom method
pair_coeff * * library.meam Co Ni Cr Fe Mn hea.meam Fe Ni Cr Co Mn

neighbor   2.0 bin
neigh_modify    delay 10 check yes

variable   Tdesird equal 77.0 #or 300K or 600k
############################
# Equilibrating
############################

thermo                100
thermo_style    custom step temp ke etotal press lx ly lz
```

```
velocity       all create ${Tdesird} 5812775
fix                1 all npt temp ${Tdesird} ${Tdesird} 1.0 iso 0.0
0.0 1.0 #isothermal-isobaric ensembles
run                   40000 #timestep= 0.001 picoseconds,40 picoseconds
unfix           1

################################################
# Mechanical Deformation Run
################################################

reset_timestep 0
change_box all boundary p s p #changing the boundary conditions

################################################
#Top and bottom clamped regions
#The other atoms are mobile
################################################

variable   bottomy equal -310 #slightly changes for each GB
variable   topy equal 310     #slightly changes for each GB
variable    lbox equal ${topy}-${bottomy} #length of the box in y
variable      limitbottom equal ${bottomy}+25 #25 A fixed
variable      limittop equal ${topy}-25 #25 A fixed

#defining the top and bottom fixed regions
region lower block INF INF INF ${limitbottom} INF INF units box

#the geometry is defined in simulation box units
# A box value selects standard distance units as defined by the units
#command, e.g. Angstroms for units = real or metal. A lattice value
#means the distance units are in lattice spacings. The lattice command
#must have been previously used to define the lattice spacings.

region upper block INF INF ${limittop} INF INF INF units box

group         lower region lower
group          upper region upper
#grouping the upper and lower fixed regions
group           boundary union lower upper
#defining the dynamic atoms
group           mobile subtract all boundary

#####################################
variable strrate equal 0.0005 #strain rate=0.0005/psec=5*(10^8)/s
variable   vyvalue equal ${strrate}*${lbox-50} #velocity A/psec
#240000 steps are sufficient to get to strain of 0.12
#considering the experimental results strain 0.5
#Nsteps (0.5/strain rate)/dt
variable Nsteps equal 1000000
variable   ThermoOut equal 1000
variable   DumpFreq equal 2000
variable   NoutAvg equal ${ThermoOut}/100
```

```
thermo          ${ThermoOut}
thermo_style    custom     step temp ke etotal press pxx pyy pzz lx ly
lz

#each component of the force on atoms of the group are set to 0
fix                   2 boundary setforce 0.0 0.0 0.0
#lower set velocity is set to zero as the lower part is not moving
#The units keyword is used by set and ramp. If units = box, the
#velocities and coordinates specified in the velocity command are
#in the standard units described by the units command (e.g.
#Angstroms/fs for real units). If units = lattice, velocities are
#in units of lattice spacings per time (e.g. spacings/fs) and
#coordinates are in lattice spacings.
velocity   lower set 0 0 0 units box
#the upper gripped part has a velocity in the y direction
velocity   upper set 0 ${vyvalue} 0 units box
#the mobile part velovity ramps up
velocity   mobile ramp vy 0.0 ${vyvalue} y ${bottomy} ${topy} sum yes
units box

fix            10 all npt temp ${Tdesird} ${Tdesird} 1.0 x 0.0 0.0 1.0
z 0.0 0.0 1.0 couple xz


dump       mydump     all   atom  ${DumpFreq}     LoadingFrame_*.dump
dump_modify     mydump     sort  id

run ${Nsteps}
```